

Performances of multi-gap timing RPCs for relativistic ions in the range $Z=1-6$

P. Cabanelas^a, M. Morales^a, J. A. Garzon^a, A. Gil^b, D. Gonzalez-Diaz^{c*}, A. Blanco^d, D. Belver^a, E. Casarejos^d, P. Fonte^{de}, W. Koenig^c, L. Lopes^d, M. Palka^c, J. Pietraszko^c, M. Traxler^c and M. Weber^f

^a *Universidade de Santiago de Compostela (USC), Santiago de Compostela, Spain*

^b *Instituto de Física Corpuscular (CSIC-UV), Valencia, Spain*

^c *Gesellschaft für Schwerionen Forschung (GSI), Darmstadt, Germany*

^d *Laboratório de Instrumentação e Física Experimental de Partículas (LIP), Coimbra, Portugal^e
Instituto Superior de Engenharia de Coimbra (ISEC), Coimbra, Portugal*

^f *Technische Universität München (TUM), Munich, Germany*

E-mail: D.Gonzalez-Diaz@gsi.de

ABSTRACT: We present the performance of Multi-gap timing RPCs under irradiation by fully stripped relativistic ions ($\gamma\beta=2.7$, $Z=1-6$). A time resolution of 80 ps at high efficiency has been obtained by just using standard ‘off the shelf’ 4-gap timing RPCs from the new HADES ToF wall. The resolution worsened to 100 ps for ~ 1 kHz/cm² proton flux and for ~ 100 Hz/cm² Carbon flux. The chambers were operated at a standard field of $E = 100$ kV/cm and showed a high stability during the experiment, supporting the fact that RPCs are a convenient choice when accommodating a very broad range of ionizing particles is needed.

The data provides insight in the region of very highly ionizing particles (up to $\times 36$ mips) and can be used to constrain the existing avalanche and Space-Charge models far from the usual ‘mip valley’. The implications of these results for the general case of detection based on secondary processes (n , γ) resulting in highly ionizing particles with characteristic energy distributions will be discussed, together with the nature of the time-charge correlation curve.

KEYWORDS: multi-gap timing RPCs; time of flight; ion detection; highly ionizing particles.

*Corresponding author

Contents

1. Introduction	1
2. Experimental setup	3
2.1 The RPC cells	3
2.2 The trigger and reference system	5
2.3 Prompt charge determination	6
2.4 Total charge and rate determination	7
2.5 The physical environment	8
2.5.1 C ¹² beam	8
2.5.2 Proton beam	11
2.5.3 Cosmic rays	12
3. Results	12
3.1 Performance of the reference system	12
3.2 RPC performance	13
3.2.1 Charge distribution	15
3.2.2 Dependence with HV	16
3.2.3 Dependence with particle rate	17
4. Dependence with particle type	19
4.1 Introduction	19
4.2 Charge distribution	19
4.3 Time distribution	21
5. Discussion	22
5.1 Element identification	22
5.2 Time-Charge correlation	24
5.3 Space-Charge	26
5.4 Streamers	27
6. Conclusions	28

1. Introduction

The development of large-scale sub-100 ps resolution RPCs has launched a number of applications in Particle and Hadron Physics, notably HARP (PS) and ALICE (LHC), STAR (RHIC), FOPI, HADES (SIS18) and CBM (SIS100) [1, 2, 3, 4, 5, 6]. The rapid progress of the field ever since its

birth [7, 8] largely lies on the invention of the multi-gap [9], the improvement in the gap definition quality that allowed to build an RPC at the 100 ps- σ scale for the first time [10] and the extension of the concept to long counters up to 1.6 m [11]. Detectors of this family are sometimes referred as Multi-gap timing RPCs¹, hereafter denoted simply by MtRPCs. All the so far existing large walls based on MtRPCs emphasize the detector response for mips at moderate particle fluxes (below 1 kHz/cm²) that are typical environments either in high energy collider experiments or low energy fixed-target ones.

There is, nonetheless, a broad range of newly born applications where MtRPCs need to work in highly ionizing environments. Maybe the most remarkable one is the detection of annihilation γ 's for Positron Emission Tomography (PET) [12] (based on the detection of the secondary electron (by Compton or photo-electric effect)). More recently, in the framework of the R³B collaboration, two main projects started R&D aimed at building large ToF walls for neutron and ion detection, respectively [13, 14]. Both of them will have to deal with a yet unexplored range of highly ionizing particles.

Remarkable success has been achieved in describing the behavior of these chambers through first principle avalanche simulations, revealing the main role of a very strong avalanche Space-Charge [15, 16, 17]. Despite the presence of this complicated phenomena, a handful of analytical expressions can be obtained if standard avalanche evolution is assumed to happen up to the threshold level [17, 18, 19, 20, 21]. The developed formalisms allow to estimate the influence of the ionization loss, hereafter referred in mips units ($\Delta E/\Delta E_{mips}$) as:

$$\bar{t}(\Delta E) = \frac{t_{rise}}{\ln 9} \ln \frac{\Delta E_{mips}}{\Delta E} + t_{off}(n_{th}, t_{rise}) \quad (1.1)$$

$$\sigma_T(\Delta E) = K_1 \frac{t_{rise}}{\ln 9} \sqrt{\frac{\Delta E_{mips}}{\Delta E}} \quad (1.2)$$

$$\varepsilon(\Delta E) = 1 - \exp \left[-n_o \left(1 - \frac{\eta}{\alpha} - \frac{\ln(1 + \frac{(\alpha-\eta)}{E_w} n_{th})}{\alpha g} \right) \frac{\Delta E}{\Delta E_{mips}} \right] \quad (1.3)$$

\bar{t} refers to the average and σ_T to the rms of the time response distribution (for the sake of simplicity it has been assumed to be Gaussian, so that \bar{t} can be thought of as the maximum of the time response distribution and σ_T equals its rms). n_{th} is the electronics threshold in number of electrons, n_o is the total number of primary ionizations for mips, g the gap size, α and η the multiplication and attachment coefficients, E_w the weighting field and K_1 is an adimensional constant of order unity that contains the effect of avalanche multiplication statistics. The signal rise-time t_{rise} is related to the coefficients of the electron swarm as:

$$t_{rise} = \frac{\ln 9}{(\alpha - \eta)v_e} \quad (1.4)$$

in absence of Space-Charge (see [20] for a discussion). The average electron drift velocity is denoted by v_e . Typical values of $t_{rise} \simeq 200$ -250 ps at threshold level have been measured with a careful setup [22, 23], for typical operating fields of $E = 100$ kV/cm, and threshold levels of

¹Also simply Multi-gap RPCs or timing RPCs. Nevertheless, it must be mentioned that high time resolution is not a property of the Multi-gap technology while high efficiency is also not a property of single gap timing RPCs.

$q_{th} = n_{th}q_e \simeq 10$ fC. It must be noted that, within the models, eq. 1.1 is generally exact, being eq. 1.2 full-filled in the limit $\Delta E/\Delta E_{mips} \rightarrow \infty$ and, contrary, eq. 1.3 for $\Delta E/\Delta E_{mips} \rightarrow 1$ (otherwise the latter must be re-interpreted as a lower limit [21]). Despite the development of analytical tools, no systematic attempt was done to clarify these dependences with exception of the controverted data from [24] and [25], that will be re-visited here, and the much too short survey of [18] (only 2 points).

The detection of ions up to $A = 200$ ($Z \simeq 100$) over large surfaces ($\simeq 5$ m²) at relativistic kinetic energies $E_K = 700$ GeV/A has recently brought attention in the R³B experiment, proposed within the new Facility for Anti-proton and Ion Research (FAIR) at Darmstadt, Germany [13]. In view of this potential new application, we conducted systematic measurements at GSI-SIS18 for evaluating the detector response under ions up to charge state $Z = 6$. Complementary, measurements with a highly mono-energetic diffuse proton beam ($E_K = 1.76$ GeV, $\sigma_{E_K}/E_K = 4\%$) and cosmic rays were also performed. Spare cells from the HADES system were used [26] and comparisons to previous results will be referred when appropriate.

Importantly, parallel plate geometries (of the kind of PPACs) have been used for many years for detecting ions at the 100 MeV energy scale or below with great success [27, 28, 29]. Apart from extending the time resolution below 100 ps, the introduction of the RPC technology should greatly improve the chamber stability and ease its construction, being intrinsically ‘spark-protected’ at ambient pressure. As shown in this work, these features are already provided by typical MtRPC designs if ions have enough energy to penetrate in a relatively bulky detector ($\simeq 20\%X_o$ here) and ion fluxes are below 1 kHz/cm².

The structure of the paper is as follows: the three different experimental setups are explained in section 2, the behavior as a function of HV and rate is presented in section 3, while section 4 is devoted to the behavior as a function of particle type, a discussion follows in section 5 about the practical use of such a counter in a highly ionizing environment and finally in section 6 we summarize our conclusions.

2. Experimental setup

2.1 The RPC cells

Two RPC cells from the new HADES MtRPC wall have been used and allocated inside their corresponding shielding profiles (acting as Faraday cages) in a custom designed aluminum gas box. As compared with the HADES system, the gas box was lacking of an optimized PCB for signal feed-through of $Z_o = 50\Omega$ (characteristic impedance) while the routing of the signals inside the box was such that they could be read out from the same box side. Electrical isolation of signal cables was ensured whenever possible in order to reduce cross-talk. A picture of a typical cell is shown in Fig. 1, consisting of 4 gaps of 0.28 mm thickness, with 2 mm thick aluminum and float glass plates. The dimensions of the cells were 22×140 mm² (width \times length), corresponding to the low polar angle region of the HADES wall. Technical details can be found in [5].

The read-out was based on the HADES FEE electronics that provides $\times 40$ amplification factor in signal amplitude at 2 GHz bandwidth [30]. The detector was read out in single-ended mode, with a signal being taken from the central electrode (anode) after filtering the HV level. No special

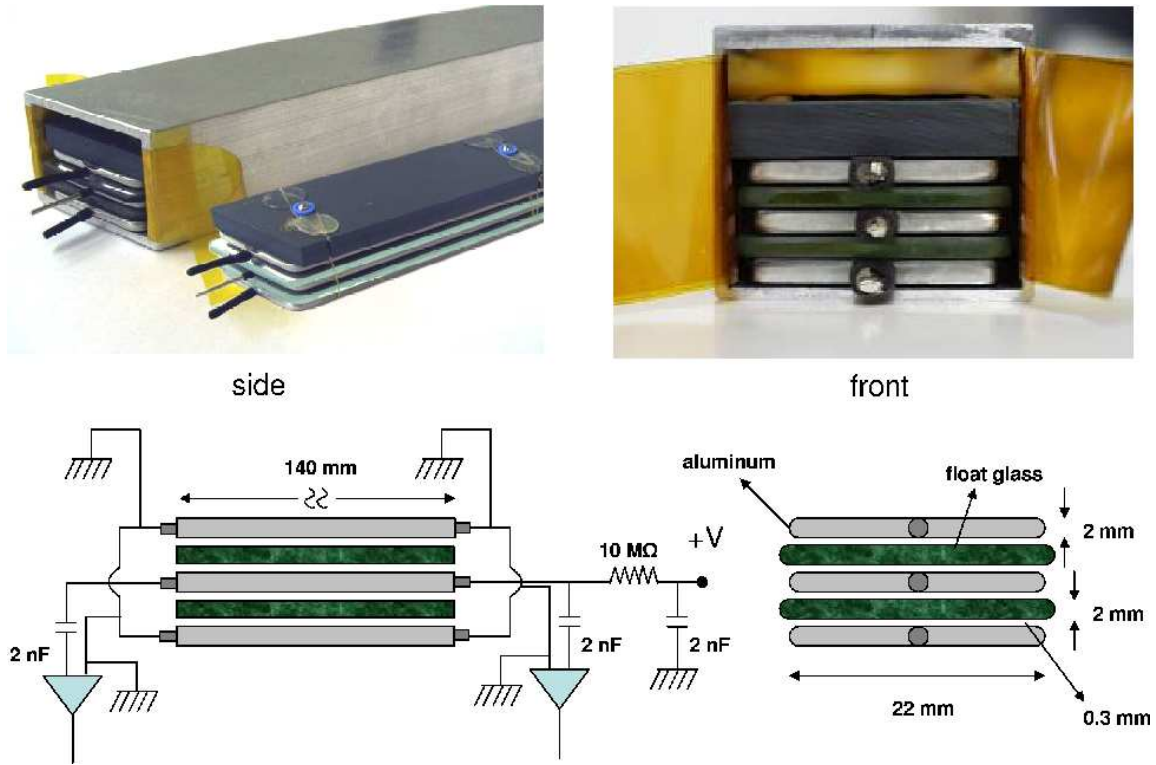


Figure 1. Up: pictures showing a typical HADES cell, before and after being placed in its corresponding Faraday cage. Down: side and front sketch of a HADES cell together with the electrical scheme used for these measurements.

care was taken for matching the detector impedance ($Z_d = 12 \pm 2\Omega$) to the coaxial LEMO cables used for signal transmission ($Z_o = 50\Omega$), while the FEE built-in dead-time of the order of 50-70 ns provided stability to the electronic chain by avoiding re-triggers caused by reflections. 2 MBs (Mother-Boards) and 2x2 DBs (Daughter-Boards) [31] fed by a customized low-ripple distributed LV system [32] were used for reading-out 8 electronic channels (2×2 RPC cells and 2×2 reference scintillators). The RPC-FEE thresholds were set to $v_{th} = 50$ mV (equivalently $v_{th} = 50/40 = 1.25$ mV and $q_{th} \simeq 30$ fC at the pre-amplifier input) and were not changed during the measurements. The gas box was used as a central ground node being the FEE, HV and cathode strips connected to it by screws and/or conductive meshes. With this grounding scheme the external noise levels were still modest and indeed for $v_{th} < 20$ mV some channels were unstable. The digitization and event building was done with the Trigger and Readout Board (TRB) developed in [33] and based on the HPTDC ASIC chip.

The oxygen content measured at the output of the gas box was below 200 ppm (measured with an Oxygen Transmitter O2X1 of GE Infrastructure Sensing) for a gas flow of 150 cc/min of an isobutane-free gas mixture based on $C_2H_2F_4/SF_6$ (90/10). Due to the high electro-negativity of the gas mixtures used for timing such ppm levels are not expected to influence the detector behavior.

2.2 The trigger and reference system

The arrangement of the RPC cells and reference scintillators is shown in Fig. 2. Two fast Bicron scintillators BC-420 and BC-422 read out in both ends by Hamamatsu H6533 photo-multipliers (PMs) were used for providing trigger, reference time and track selection for efficiency studies. The scintillator-PM assembly was placed inside PVC tubes of 50 mm diameter and optical silicone was applied to the contact surface scintillator-PM while the scintillator was wrapped in silver paper to improve light transmission. Such a detector choice had previously yielded $\sigma_r = 35$ ps per counter for mips [11].

For the scintillators readout the HADES FEE was also used with the pre-amplifier being bypassed in virtue of the PM amplification. The PMs were operated at a nominal voltage $V = -2.2$ kV for which the average signal amplitude was just slightly higher than that of RPC signals after amplification. Variations around the nominal voltage were introduced to account for slight differences in the characteristic gain curves of the different PMs. The same threshold as in the RPC-FEE was used.

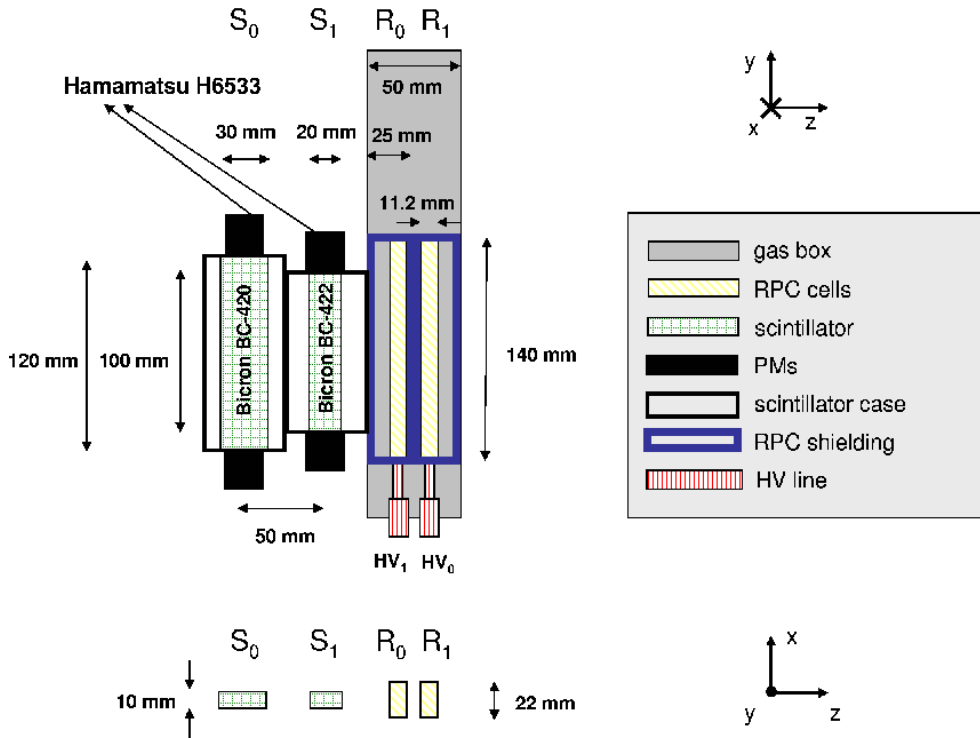


Figure 2. Different views of the arrangement of the reference scintillators and RPC cells used for the measurements.

We have chosen a setup with the 4 counters (2 RPCs and 2 scintillators) being placed vertically along their longest side. The scintillators, being prisms of dimensions $10 \times 20 \times 100$ mm³ (BC-422) and $10 \times 30 \times 120$ mm³ (BC-420) were stacked over their narrower faces (10×100 mm² and 10×120 mm², respectively). They could be aligned with an estimated precision of the order of ± 2 mm. A similar procedure was followed with the RPC cells. Being mechanically identical and placed inside aluminum profiles, both RPC cells can be easily stacked with a mutual alignment

better than 1 mm. The reference system was carefully centered with respect to the RPCs in order to provide a good reference for efficiency estimates. Requesting an additional coincidence with one of the ('reference' in such case) RPC is expected to compensate for any error on the aforementioned procedure and was done when possible (measurements of section 2.5.2).

For all the measurements the trigger was provided by a coincidence of the 4 PM output signals. In order to do that the PM outputs were split, with one being sent to a Leading Edge Discriminator (LED) while the other was fed directly into the FEE after by-passing the amplifier, both discriminators having the same threshold.

Additionally to the scintillator reference system, two fast position sensitive mono-crystalline diamonds were placed 14 m upstream, roughly at the focal plane of the last HADES beam-line quadrupole. The surface dimensions of the detectors were $4.7 \times 4.7 \text{ mm}^2$ and $3.5 \times 3.5 \text{ mm}^2$ and their individual time resolutions in the range 100-150 ps [34]. Although not in the trigger because of technical reasons, a coincidence probability of 10% was observed off-line, allowing for an improved track selection and energy spread determination. Those were used only in a reduced set of the measurements (section 2.5.2).

2.3 Prompt charge determination

The electron induced (prompt) charge q_p was codified in the width of the FEE (LVDS) output signal through a 'charge to width' algorithm [30], that will be referred as $QtoW$. The algorithm is non-linear as illustrated in Fig. 3 with avalanches lying mainly on a first (steep) linear part of the $QtoW$ vs q_p correlation curve, while streamers are concentrated in a second (soft) one. Despite the non-linearity, avalanches and streamers can be well resolved (Fig. 3-right) and appear separated at around $q_p \simeq 5 \text{ pC}$ ($QtoW = 200 \text{ ns}$). This 'QtoW method' can indeed accommodate a very large dynamic range while keeping the charge resolution below 10% - σ for avalanche-like pulses with $q_p > 50 \text{ fC}$. (Fig. 3-left, dot-dashed line). Points in Fig. 3-left were obtained by injecting the charge with a fast square pulser ($t_{rise} = 0.35 \text{ ns}$) after differentiation ($C = 1 \text{ nF}$, $R = 50\Omega$) in order to emulate the shape of the RPC signals. Data was taken with a Tektronics TDS7104 Oscilloscope (BW=1GHz).

The bi-linear behavior of the average signal width (\overline{QtoW}) as a function of the average prompt charge (\bar{q}_p) can be embodied in a simple parameterization as:

$$\overline{QtoW} = a(1 - e^{-b\bar{q}_p}) + c\bar{q}_p + QtoW_{min} \quad (2.1)$$

after which the resolution of the 'QtoW method' can be obtained:

$$\frac{\sigma_{q_p}}{\bar{q}_p} = \frac{\partial \bar{q}_p}{\partial \overline{QtoW}} \frac{\sigma_{QtoW}}{\bar{q}_p} \quad (2.2)$$

$$\frac{\sigma_{q_p}}{\bar{q}_p} = \frac{1}{abe^{-b\bar{q}_p} + c} \frac{\sigma_{QtoW}}{\bar{q}_p} \quad (2.3)$$

$QtoW_{min}$ (53 ns for the channel shown in Fig. 3) is the minimum output signal width, corresponding to the minimum time during which the comparator is being self-latched. By numeric integration of the signal amplitude, a close agreement for the $QtoW$ vs q_p curves was observed when analyzing avalanches originated inside the detector as compared with pulser data, while streamers clearly

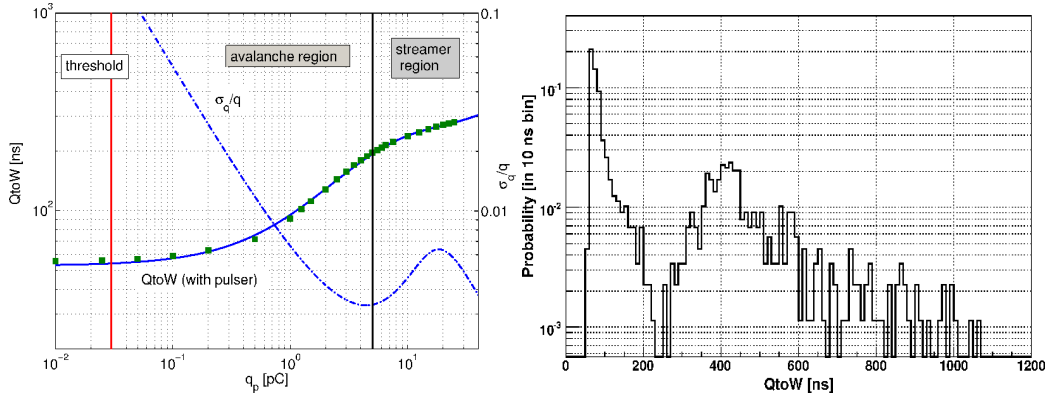


Figure 3. Left: average behavior of the output signal width ($QtoW$) as a function of the input pulser charge together with a 4-parameter fit. The avalanche and streamer regions are indicated and also the threshold level. The dot-dashed line shows the charge resolution resulting from the fit after including the fluctuations in the $QtoW$ value (right axis). Right: $QtoW$ distribution measured in the RPC under cosmic rays for an operating voltage $V = 6.0$ kV. The two separate distributions can be attributed to avalanches and streamers.

deviate from the pulser behavior (up to a factor 1/2 less in the reconstructed q_p). The fluctuations of the signal width are of the order of $\sigma_{QtoW} = 200$ ps and no dependence with the input charge was observed. A detailed description of the performances of the final HADES-FEE will be the subject of a more technical forthcoming publication and will not follow in this paper.

Eq. 2.1 provides an accurate phenomenological description and illustrates the different behavior of the algorithm for low and high charges, but cannot be inverted, so in practice a σ^h order polynomial was used to obtain the ‘calibration curve’ $q_p(QtoW)$. To avoid errors resulting from an incorrect extrapolation, values of the signal width in excess of 290 ns are considered as an ‘overflow’ and the maximum pulser charge of $q_p = 25$ pC is assigned to them. Such big charges are rarely achieved under ordinary circumstances and they occurred seldom even in the very harsh environment studied here.

2.4 Total charge and rate determination

The dynamic behavior of an RPC at high rates is bound to the average total avalanche charge \bar{q}_T [35, 36]. Being readily obtainable by a direct current measurement (after dividing by the avalanche rate), its value is directly related to the average gap voltage once the stationary (DC) situation is reached, as:

$$\bar{V} = V - \bar{I}R = V - \bar{q}_T \Phi \rho d \quad (2.4)$$

with Φ the avalanche flux [in Hz/cm²], ρ the electrode resistivity and d its thickness. V is the applied voltage, \bar{I} the average current and R the electrode resistance. As compared with the stationary (DC) situation described by eq. 2.4, the interpretation of $\bar{q}_T(t)$ during the stabilization of the field in the gap is more intricate [37]. Although it is not the main focus of the present work to study the transient behavior of the RPC cells, proper means for determining the average avalanche charge as a function of the irradiation time were devised as follows. The particle rate was measured from scintillator S_1 as the coincidence of signals from its two PMs. This provides an unbiased rate estimate by suppressing single electron noise. The coincidence signal was sent to the scaler input

of a commercial LabJack U3 acquisition board connected to a computer, and its value stored every 0.2 s. Complementary, the RPC current was measured via the analog output of a 2-channel CAEN N471A HV supply, after calibration. Although the HV-display resolution is ± 1 nA, by averaging the analog output the resolution could be improved down to $\simeq 0.5$ nA. Due to the presence of environmental noise, the measured current had to be averaged over a pretty large time interval of $\simeq 0.8$ s being stored every 0.2 s, and read-out with the same acquisition board. With the help of a second scaler input in the LabJack U3, the cycles of an external 40 kHz clock were counted in order to provide a stable time estimate.

2.5 The physical environment

2.5.1 C^{12} beam

Measurements were performed with three distinct setups. In a first one (Fig. 4a) C^{12} was injected in the experimental area at a kinetic energy $E_K = 1.8$ GeV/A directly from SIS18. The beam was focused at the usual HADES target position, 14 m upstream our reference detectors. The latter were placed close to the beam dump and optically aligned with respect to the beam-line. A typical beam profile at the level of few mm^2 was expected in the target transverse (XY) plane, from which experience tells that the transverse dimension of the primary beam amounts to some cm^2 at the beam dump. The accelerator was operated in the so-called slow extraction mode that allows for a fairly sustained beam intensity along 8 seconds spill (effectively) with a duty cycle close to 50%. Typical spill time-profiles are shown in Fig. 5 (left).

The non-perfect detector-beam alignment resulted in a position distribution over the reference scintillator system characterized by a narrow peak ($1 \text{ cm} - \sigma$) close to one of the detectors ends, submersed in an uniform background (Fig. 6-left). After selection based on the signal width in the reference scintillators (Fig. 7), the peak could be attributed to the primary C^{12} beam while the uniform background was largely populated by secondary protons and He together with species with $Z = 3, 4, 5$ (either Carbon charge states or Li, Be, B species), the latter at a much lower yield. Particles different from Carbon must have been originated along the roughly 14 meters downstream from the exit of the vacuum pipe to the detector setup. Due to the different shape of the scintillator signals as compared with RPC avalanches, the absence of amplifier and the eventual saturation of the PMs at the higher charges, the calibration curve from Fig. 3 could not be used and we present in Fig. 7 the raw values of the signal width ($QtoW$). Based on them we believe, nevertheless, that identification can be performed with little ambiguity.

The position in the scintillators was determined by constraining the width of the time difference distribution (left-right) to the known detector dimensions. In such a case the propagation velocity can be obtained as:

$$v_{prop} = 2 \frac{L}{(t_L - t_R)_{50}} \quad (2.5)$$

where $(t_L - t_R)_{50}$ refers to the width of the time difference profile at 50% drop from the flat top. The effective light propagation velocities obtained were $v_{prop,s_0} = 0.385c$ and $v_{prop,s_1} = 0.380c$, being c the speed of light. Finally, the detectors were mutually aligned by software by imposing that the average position difference $(\bar{y}_{s_0} - \bar{y}_{s_1})$ was centered at zero.

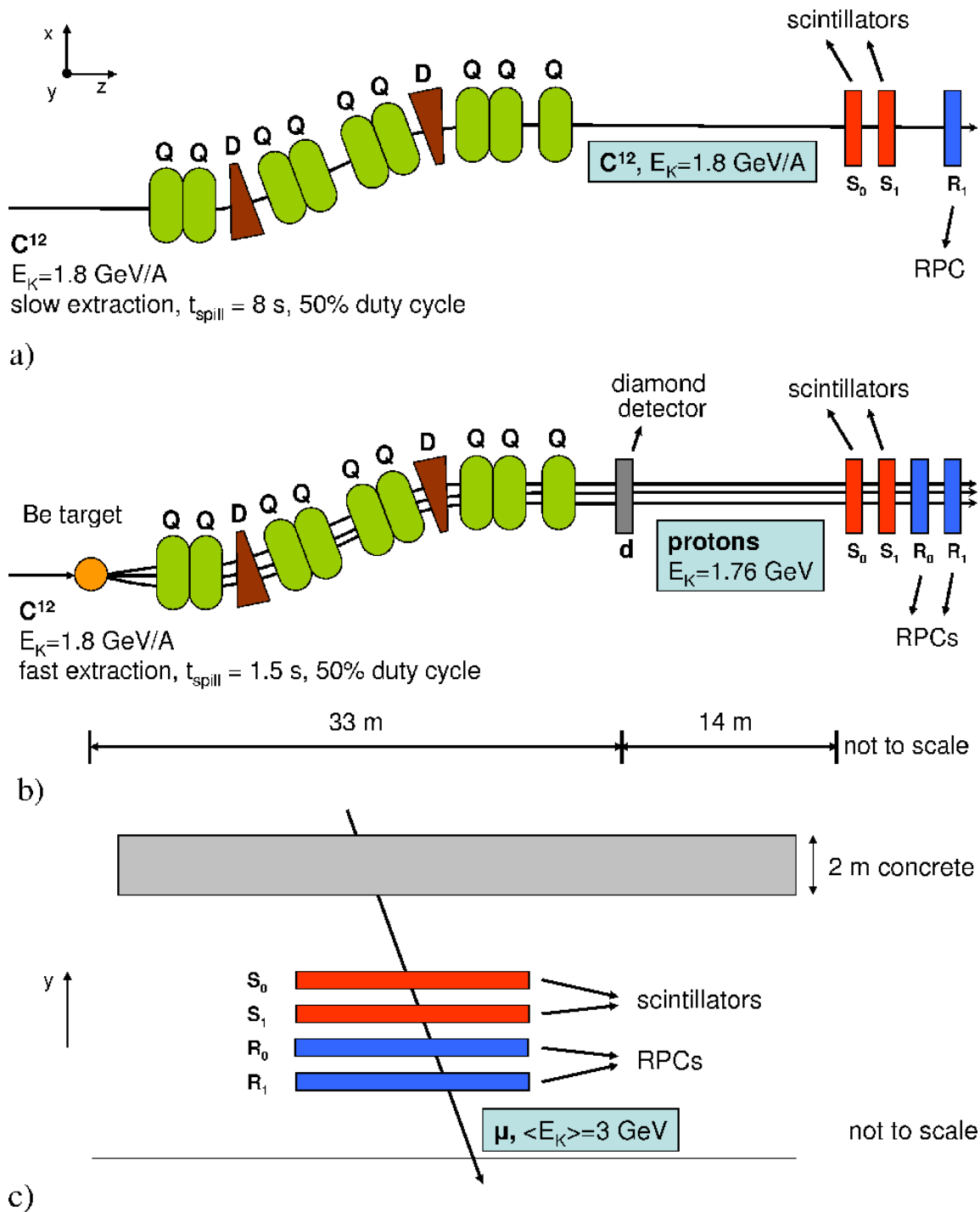


Figure 4. a) Setup for focused C^{12} irradiation (kinetic energy $E_K = 1.8 \text{ GeV/A}$, $\sigma_{E_K}/E_K < 1\%$). b) Setup for diffuse proton irradiation ($E_K = 1.76 \text{ GeV}$, $\sigma_{E_K}/E_K = 4\%$) after C^{12} reactions in a secondary Beryllium target placed 33 m upstream the experimental hall. Diamonds have been added and also a second RPC (R_0). c) Setup for cosmic muon detection.

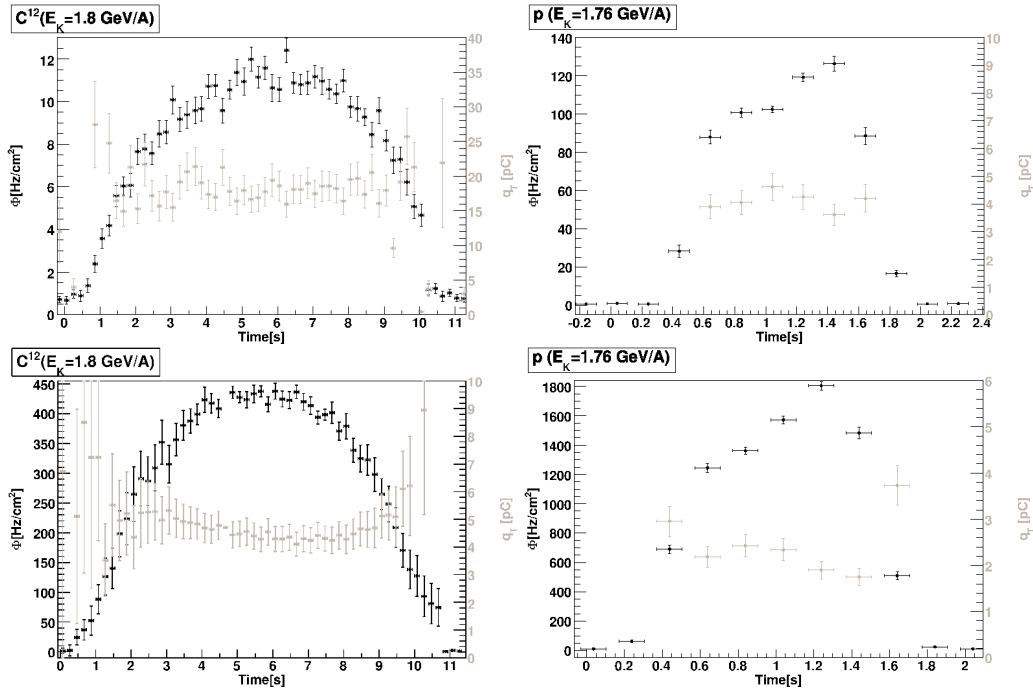


Figure 5. Illustration of characteristic spill time-profiles. The left column shows the average flux profile (over many spills) and the average total charge \bar{q}_T behavior (right axis) for illumination with C^{12} (kinetic energy $E_K = 1.8$ GeV/A) at two different beam intensities. Right column shows similar plots for diffuse proton illumination ($E_K = 1.76 \pm 4\%$ GeV). The extraction time was about a factor 5 smaller in such a case. The transient behavior is little visible since the measured current had to be averaged over a pretty large time-interval of 0.8 s due to external noise.

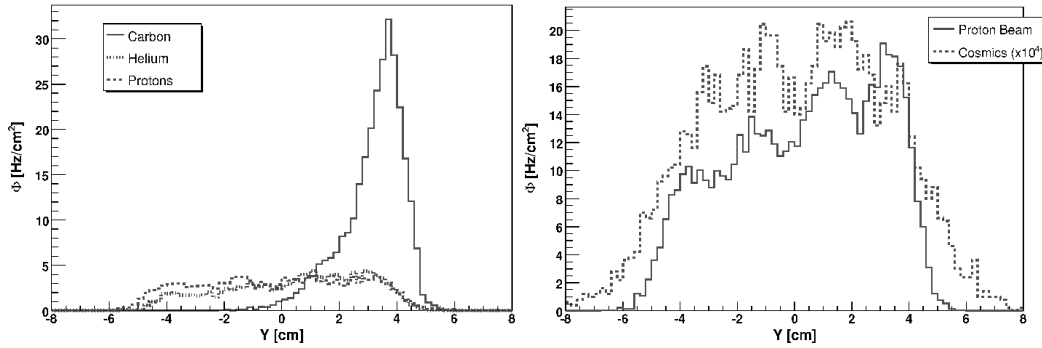


Figure 6. Left: Position distribution along the reference scintillator S_o under C^{12} illumination. The proton, He and C^{12} curves are shown after charge selection, manifesting the primary C^{12} beam (kinetic energy $E_K = 1.8$ GeV/A) close to the border of the reference counters. Right: Position distribution under diffuse proton illumination ($E_K = 1.76 \pm 4\%$ GeV) and cosmic ray profile (overlaid). The slightly bigger profile under cosmic rays stems from the larger angular spread (see text).

Only one RPC cell (R_1) was used during these measurements since R_o could not be powered up due to technical reasons. A constant voltage $V = 5.6$ kV was applied to the RPC, while the primary flux ranged from 10 to 1000 Hz/cm².

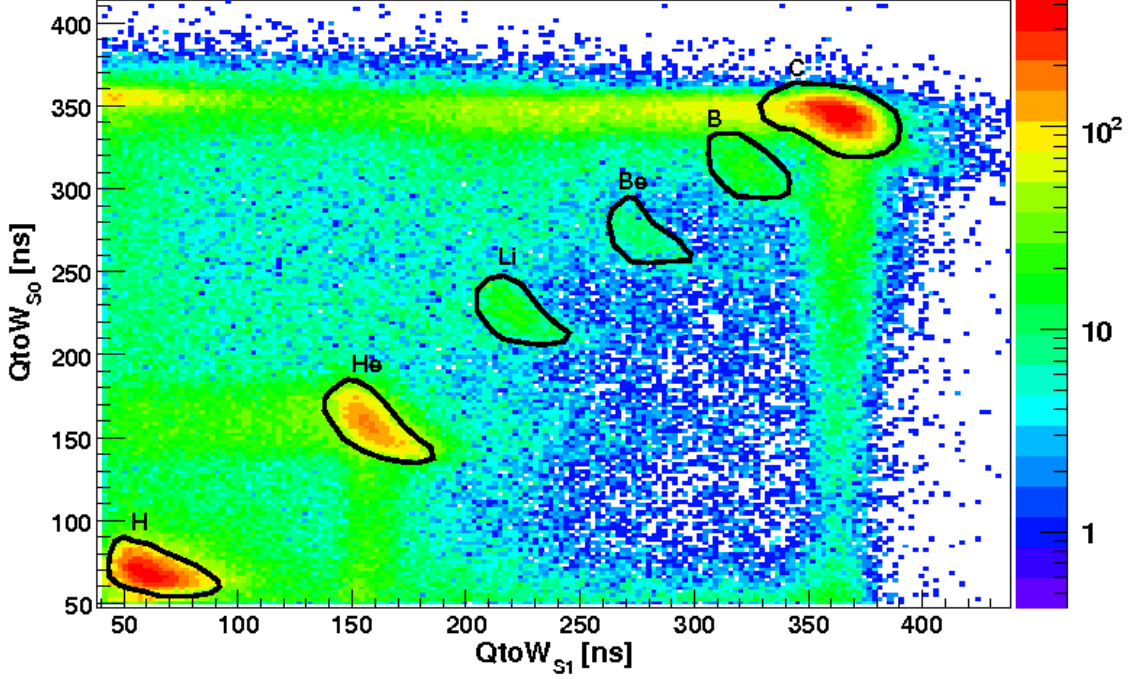


Figure 7. Two-dimensional correlation plot between the raw signal widths obtained in the reference scintillators after offset subtraction (color on-line). Six blobs can be identified being the most prominent ones attributable to protons, He and C^{12} . The other 3 blobs with a much lower yield must be Li, Be and B or charge states of the C^{12} ion.

2.5.2 Proton beam

In a second setup (Fig. 4b), C^{12} at $E_K = 1.8$ GeV/A was collided into a Beryllium secondary target placed 33 m upstream the experimental area. The magnetic field of the following dipoles and quadrupoles in the beam line was adjusted for accepting forward protons from the reaction at an average energy $E_K = 1.76$ GeV (that accounts for energy losses in the Be target itself). As a consequence of Fermi motion, protons had still a sizeable angular straggling that rendered a much more uniform irradiation than for the C^{12} beam (Fig. 6-right).

In this setup, auxiliary mono-crystalline diamonds were placed 14 m upstream the scintillator reference system. From the time spread between the diamond detector and the first scintillator, $\sigma_{T(D-S_0)} = 248$ ps, and the simultaneously measured scintillator and diamond resolutions ($\sigma_{T(D)} = 150$ ps, $\sigma_{T(S_0)} = \sigma_{T(S_1)} = 40$ ps) the energy spread of the proton beam after propagation over $D = 14$ m could be determined as:

$$\frac{\sigma_{E_K}}{E_K} = \frac{m_p}{E_K} \frac{\beta^2}{3^{3/2} \sqrt{1 - \beta^2}} \frac{\sigma_{tof}}{tof} \quad (2.6)$$

being

$$tof = \frac{D}{\beta c} \quad (2.7)$$

$$\sigma_{tof} = \sqrt{\sigma_{T(D-S_0)}^2 - \sigma_{T(D)}^2 - \sigma_{T(S_0)}^2} \quad (2.8)$$

resulting in a value for $\frac{\sigma_{E_K}}{E_K} = 4\%$. The energy losses due to the presence of 14 m of air are much below 4% for protons at this energy, supporting that the energy straggling is indeed originated in the production at the Be target. Although the time resolution of the diamonds was reduced further down to the level of 100 ps after a special analysis [34], this discussion remains out of the scope of the present paper.

The accelerator was also operated in slow extraction mode but at a reduced extraction time (1.5 seconds), resulting in a slightly asymmetric spill time-profile (Fig. 5-right). Two RPCs (R_o , R_1) were powered up and measurements were taken as a function of the particle flux in the range 10-1000 Hz/cm² at voltages from 5.0-5.8 kV.

2.5.3 Cosmic rays

We took data, after the measurements of the previous two sections were performed, in a ‘reference setup’ with a cosmic stand where the scintillators and RPC cells were assembled according to the previous section but horizontal with respect to the ground. From the 2 meters of concrete that cover the HADES experimental area it can be estimated that the main source of particles traversing the 4 detectors are muons at an average energy $\bar{E}_K = 3$ GeV ($\simeq 1$ GeV energy loss) [38]. The position profile obtained from scintillator S_o as shown in Fig. 6-right is fairly uniform but a bit broader than for proton irradiation, due to the larger angular straggling (since S_1 is a bit smaller than S_o and is also in trigger, for perpendicular incidence the measured S_o length is very close to the S_1 one and therefore $\simeq 2$ cm smaller than its true length). The HV was varied in the range 5.6-6.0 kV.

3. Results

3.1 Performance of the reference system

The use of LED discriminators for the reference scintillators requires of time-charge slewing corrections in order to obtain the best timing. The correlation of the time-of-flight between S_o and S_1 ($\Delta t_{S_o-S_1}$) with the average signal width is shown in Fig. 8, being:

$$\Delta t_{S_o-S_1} = \left. \frac{t_L + t_R}{2} \right|_{S_o} - \left. \frac{t_L + t_R}{2} \right|_{S_1} \quad (3.1)$$

The different species from $Z=1-6$ could be cleanly separated as shown in Fig. 7 and a time-width correction was performed individually for each specie on the basis of multi-linear segments. After this procedure, a combined time resolution of $\simeq 55$ ps was obtained for $\Delta t_{S_o-S_1}$ that, assuming both detectors to perform equally, yielded per counter $\sigma_r = 40$ ps for C^{12} , $\sigma_r = 39$ ps and $\sigma_r = 42$ ps for secondary He and p. The final time-of-flight distributions after corrections are shown in Fig. 8 for different particle species, showing a strong Gaussian behavior with $\sigma_r \simeq 40$ ps per counter, while the position resolution obtained from the position difference between the counters was $\sigma_y = 6$ mm. No dependence with the particle specie was observed. Being the values for σ_r consistent with the electronic resolution of the mean-time obtained with pulsed signals [32] and not depending on the primary ionization, provides a strong evidence that the performance of the reference system was indeed limited by the TDC resolution.

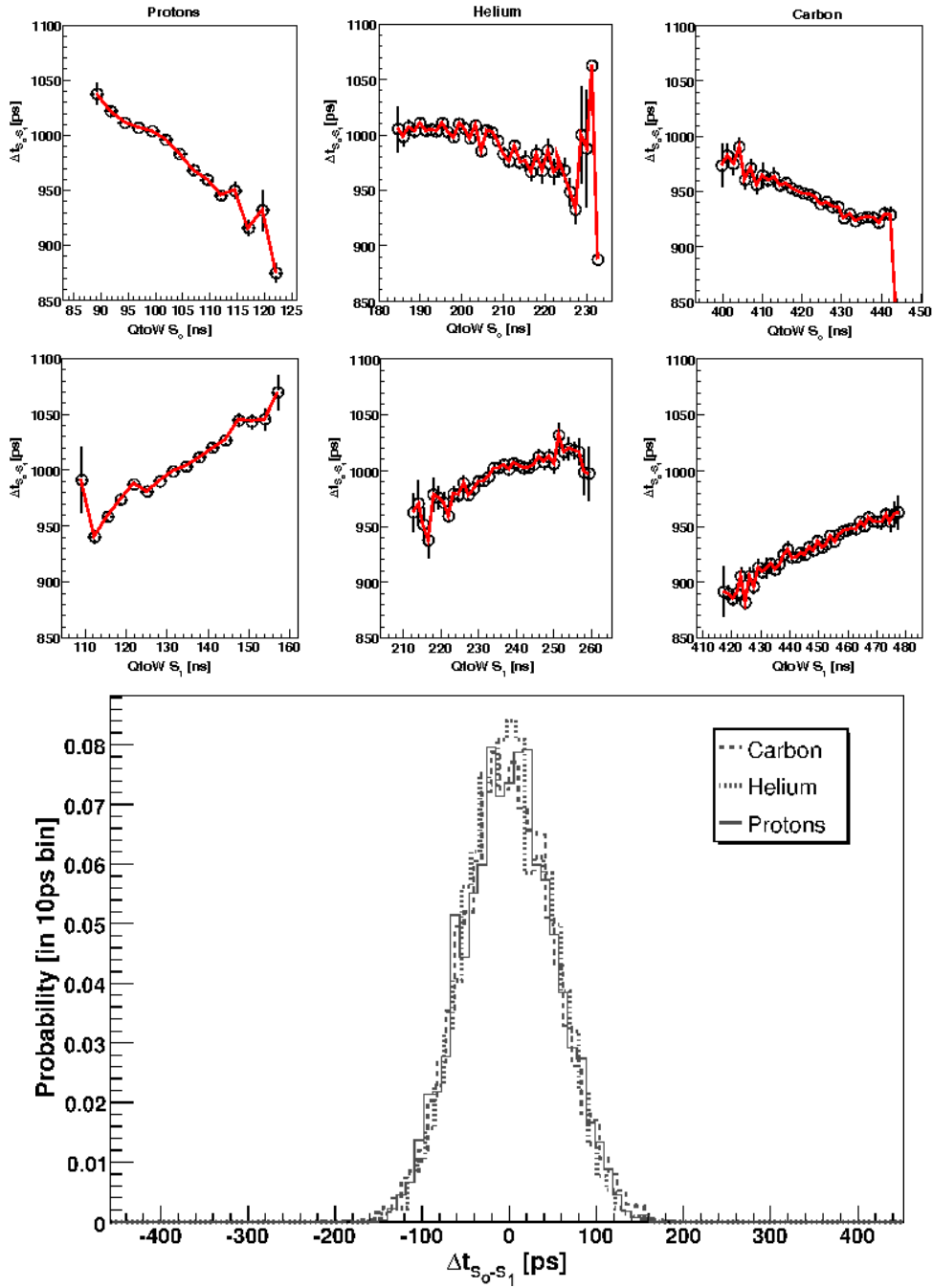


Figure 8. Up: multi-linear fit used for correcting the walk of the time of flight between the reference scintillators ($\Delta t_{S_0-S_1}$) as a function of the signal width ($QtoW$) for p, He and C^{12} . Down: distribution of times of flight between scintillators after the correction procedure for the three species.

3.2 RPC performance

The track selection was based on graphical cuts on the 2-dimensional signal width distribution in the scintillators (Fig. 7) for selecting the particle species corresponding to $Z=1-6$. Due to the

energy regime, either secondary forward protons from C^{12} up-stream reactions or primary ones with $E_K \simeq 1.76$ GeV can be highly regarded as mips ($\gamma\beta \simeq 2.7$), the latter having additionally very little energy spread. On the other hand, an estimate of the energy loss from the Bethe-Bloch formula (eq. 4.1) indicates that cosmic muons with $E_K \simeq 3$ GeV ($\gamma\beta \simeq 30$) can ionize 30% more in the RPC gas than mips. A normalized charge distribution after cuts is shown in Fig. 9 where indeed a very small difference is seen between the 3 different cases, being the average charge released by cosmic muons a bit higher, indeed, than that for mips.

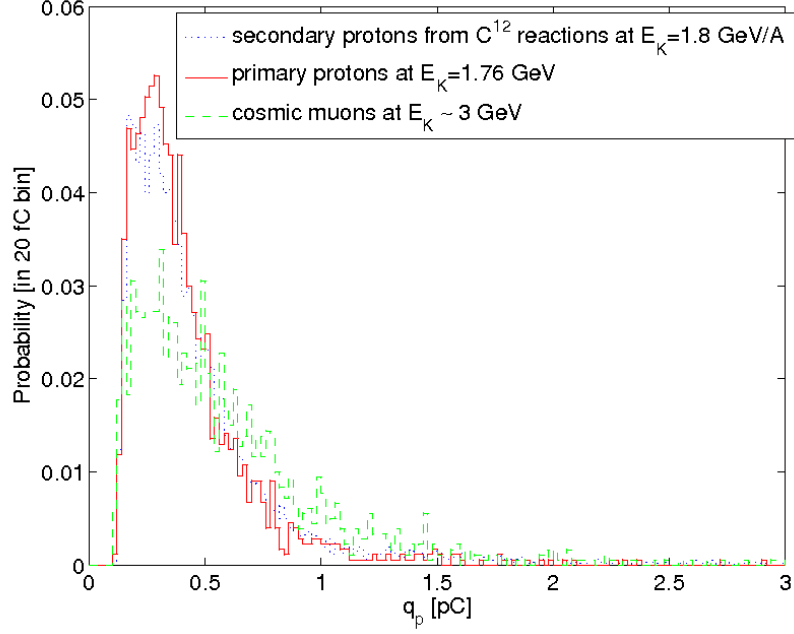


Figure 9. Comparison of the charge distribution measured in the RPC under a diffuse proton beam at a kinetic energy $E_K = 1.76$ GeV $\pm 4\%$ (continuous line), secondary forward protons from C^{12} interactions at $E_K \sim 1.8$ GeV (dotted) and cosmic muons at $E_K \sim 3$ GeV (dashed).

After particle identification, the last 1 cm from the border of the scintillators was disregarded. Furthermore, a ‘co-linearity’ cut of $\pm 2\text{-}\sigma$ in the distribution of the position differences between scintillators ($y_{s_0} - y_{s_1}$) was applied for improving the track quality selection. In order to reduce the effect of the non-uniform irradiation, C^{12} ions were additionally selected by a cut at $y > 2$ cm and other species by $y < 0$ cm. After these cuts for enhancing the purity and quality of the reference tracks, the time of flight between the two overlapping RPCs ($\Delta t_{R_0-R_1}$) was defined:

$$\Delta t_{R_0-R_1} = \left. \frac{t_L + t_R}{2} \right|_{R_0} - \left. \frac{t_L + t_R}{2} \right|_{R_1} \quad (3.2)$$

and the time resolution per counter was obtained as $\sigma_T = \sigma_{\Delta t_{R_0-R_1}} / \sqrt{2}$. Correction curves with respect to the charge of both RPCs (slewing correction) and the position as given by the scintillators were performed. This is discussed in detail in section 5.2. A typical time-of-flight distribution for protons at an uniform flux of 150 Hz/cm² is shown in Fig. 10, yielding $\sigma_T = 87$ ps per RPC. We

applied the usual recursive fit around $\pm 1.5\text{-}\sigma$ to reduce the influence of tails in the fit [11], but for this set of measurements the value of σ_T changed little indeed if a direct fit was performed.

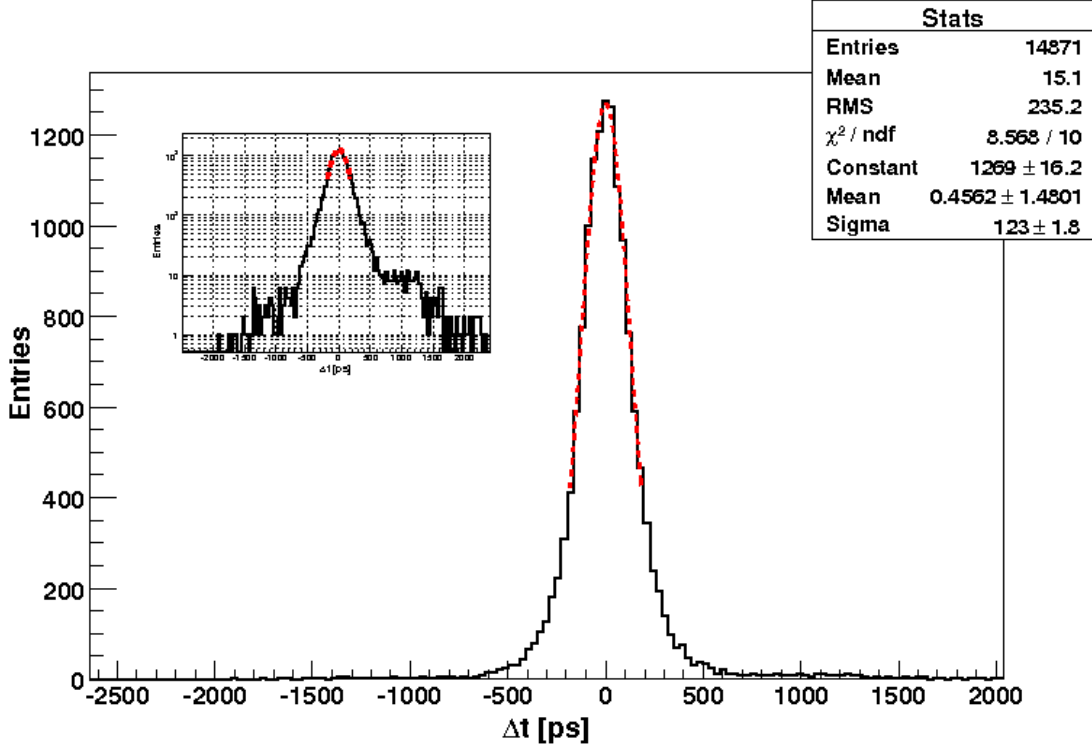


Figure 10. Time of flight distribution between RPCs for a diffuse proton beam (kinetic energy $E_K = 1.76 \text{ GeV} \pm 4\%$) at 150 Hz/cm^2 and $V=5.6 \text{ kV}$. The inset shows the same distribution in logarithmic scale, indicating the presence of tails at 1% level. The counter resolution from the fit is $\sigma_r = 123/\sqrt{2} = 87\text{ps}$.

In the C^{12} experiment, due to the absence of the RPC cell R_o , the time difference with respect to scintillator S_o was calculated in a similar manner:

$$\Delta t_{R_1-S_o} = \left. \frac{t_L + t_R}{2} \right|_{R_1} - \left. \frac{t_L + t_R}{2} \right|_{S_o} \quad (3.3)$$

and the RPC resolution obtained after subtracting the contribution of the reference system: $\sigma_r = \sqrt{\sigma_{\Delta t_{R_1-S_o}}^2 - \sigma_{\Delta t_{S_o-S_1}}^2} / 2$.

3.2.1 Charge distribution

Normalized charge distributions are shown in Fig. 11 for $Z = 1-6$ at $V = 5.6 \text{ kV}$ at low rates ($\phi < 10 \text{ Hz/cm}^2$). A phenomenological fit to 4-parameter Landau-like distributions

$$\mathcal{P} = a \exp(-bq_p - ce^{-dq_p}) \quad (3.4)$$

provides a good description and partially captures the high charge tails. Fig. 11 shows that there is indeed a strong correlation between the charge initially released and the final avalanche charge,

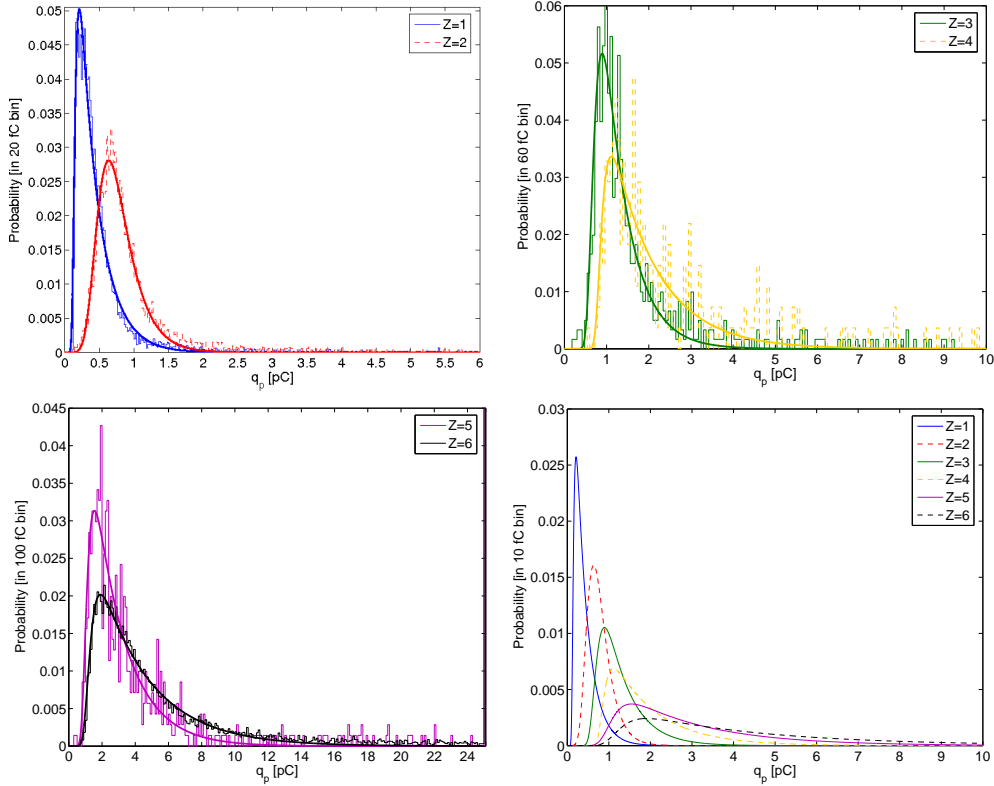


Figure 11. Up-left: RPC charge distributions for fully stripped ions with atomic charges $Z = 1, 2$ together with a fit to a Landau-like function. Up-right: $Z = 3, 4$. Down-left: $Z = 5, 6$. Down-right: Fitted curves for $Z = 1-6$. The normalized momenta is $\gamma\beta \simeq 2.7$ in all cases, $V=5.6$ kV and $\phi < 10$ Hz/cm².

but clearly not proportional, as one would expect if Space-Charge would be strong. Nevertheless, specific experimental situations where protons must be separated from Carbon, for instance, can be certainly addressed with these counters. These issues are further discussed in section 4. Remarkably, it seems not to exist a clear separation between avalanches and streamers at high initial ionizations (contrary to the case when increasing HV, see Fig. 3). This fact cannot be firmly attributed to the RPC dynamics since our charge calibration is sensitive to the signal shape and is therefore different for streamers, as pointed out in section 2.3. Due to that, the region $q_p > 5$ pC can be probably not assessed precisely in this work.

3.2.2 Dependence with HV

A scan in HV was performed for $E_K = 1.76$ GeV diffuse protons and cosmic muon irradiation. A particle flux of 150 Hz/cm² was chosen for the former while a much lower one was observed for the latter. The behavior of the time resolution and efficiency is shown in Fig. 12. Closed and open circles represent the efficiency when at least one or when both detector ends collect a valid signal, respectively, showing little difference. As compared with [26] the behavior is slightly (but consistently) worse. While the resolution at the plateau is $\sigma_r \simeq 90$ ps both for protons (diamonds) and cosmic muons (triangles), and the efficiency $\varepsilon = 92\%$ (squares) and $\varepsilon = 96\%$ (circles) correspond-

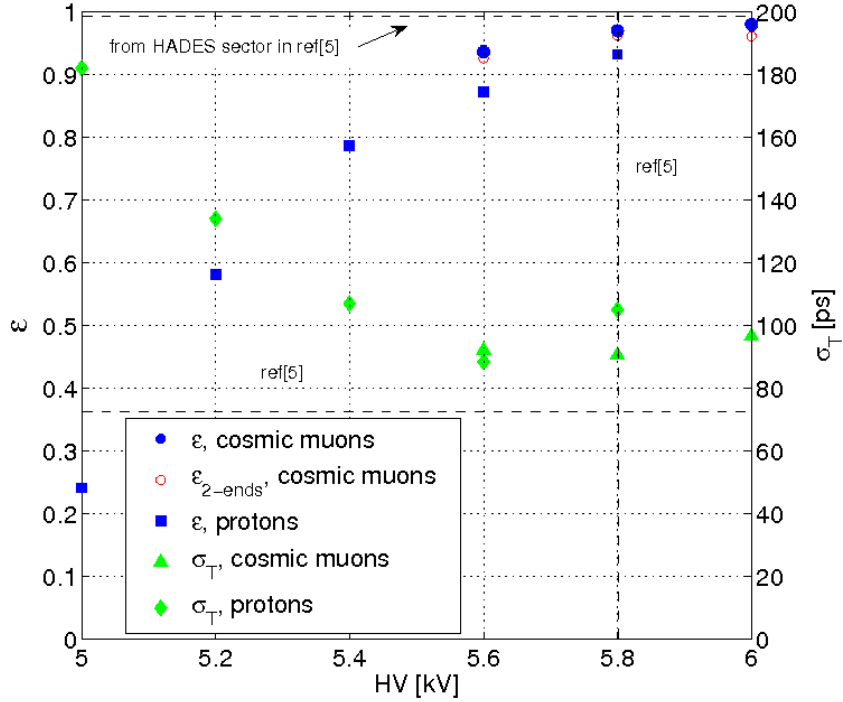


Figure 12. Efficiency for cosmic muons as a function of High Voltage when requiring a valid hit in least one detector end (full circles) or in both (open circles), together with the efficiency for $E_K = 1.76 \pm 4\%$ GeV protons (squares). Time resolution for cosmic muons (triangles) and $E_K = 1.76 \pm 4\%$ GeV protons (diamonds) is also shown with scale on the right axis. A comparison with the system values from [5, 26] (efficiency, resolution and working point) is indicated by dashed lines.

ingly, the values reported for the HADES in-beam test [26] were $\sigma_r = 73$ ps, $\epsilon = 99\%$ (intrinsic) and $\epsilon = 98\%$ (system). Nevertheless, in such a case, no particle identification was available and actually a fraction of the impinging particles is expected to be more ionizing than mips. This, together with the slight redundancy of the HADES system ($\simeq 30\%$ cell overlap) may explain the slightly worse efficiencies observed here for mips. The worse resolution may be attributed to the grounding scheme and overall noise, routing and signal feed-through (unproperly matched) as compared with [26]. The multi-peak structure observed in the time response for the lowest voltage run ($V = 5.0$ kV, $\epsilon=24\%$) suggests that the noise level was abnormally high, eventually influencing the response when the signals were very close to the threshold. This effect disappears at the nominal voltages $V = 5.6 - 6.0$ kV but a residual contribution to the overall resolution can certainly not be excluded.

The chambers showed dark rates of 0.05 Hz/cm² ($V = 5.6$ kV) and 0.15 Hz/cm² ($V = 6.0$ kV). Few minutes were needed after applying the HV before such values were reached, exceeding those by a factor 10-20 otherwise. Dark current was generally at the level of 1 nA or below.

3.2.3 Dependence with particle rate

The rate capability of 4-gap MtRPCs with metallic electrodes and 2 mm glass plates has been studied under mip irradiation before [40], yielding a 5% efficiency drop ($-\Delta\epsilon$) at 350 Hz/cm² and slight deterioration of timing performances. Another study in [41],[42] consistently showed that a

moderate 10 °C temperature increase allows to keep the time resolution up to 1 kHz/cm² at least. We present once again the behavior of the time resolution and efficiency as a function of the particle flux in Fig. 13 for a typical field $E = 100$ kV/cm, together with the fit from previous work [40] (dashed lines) and added the behavior under C¹² ions. In this last case the non-uniform irradiation is taken into account from the measured position profile (Fig. 6) through an average over ± 1 cm around the peak value. For the proton case the study was performed with a diffuse beam (section 2.5.2).

Indeed the behavior for protons as seen in Fig. 13 is similar to the one reported in [40] but with a slightly worst resolution at low rates. Clearly, the efficiency for C¹² is unaffected even at 600 Hz/cm² since the effective field drop is overcompensated by the largest initial charge (see Fig. 11). In this particular situation the resolution is expected to be more sensitive to the effective field (eq. 1.2) through $t_{rise}(\bar{E})$ and so a deterioration of the rate capability for C¹² by a factor $\times 5$ with respect to protons can be inferred from the figure (if the flux at $\sigma_r = 100$ ps is compared, for instance). Note that from eq. 2.4 one expects (at moderate rates, when \bar{q}_T changes little) this factor to be directly the ratio of the total avalanche charges $\bar{q}_{T,C^{12}}/\bar{q}_{T,p}$. If the MtRPCs would work in the proportional regime this ratio would be $Z^2 = 36$.

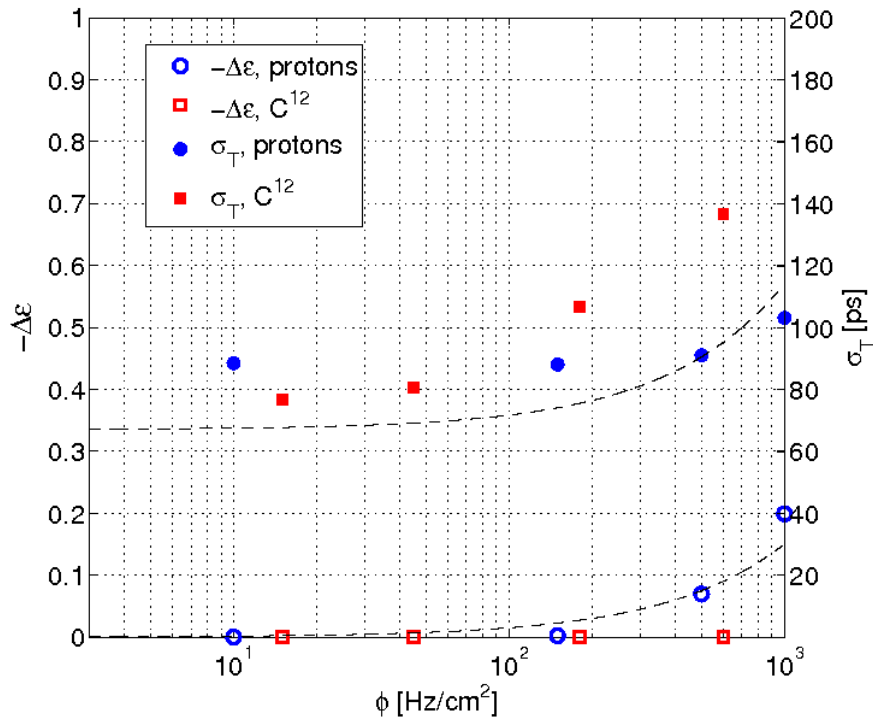


Figure 13. Time resolution σ_r and decrease in efficiency $-\Delta\epsilon$ in the RPCs for protons at $E_K = 1.76 \pm 4\%$ GeV (circles) and fully stripped Carbon ions at $E_K = 1.8$ GeV/A (squares) as a function of their flux. The operating voltage was $V = 5.6$ kV.

A remarkable fact is that for MtRPCs under mip irradiation both ϵ and σ_r begin to deteriorate at a similar value of the flux while for higher initial ionizations the former can be kept at reasonable

values even at high particle fluxes and mainly σ_r is affected.

Fig. 13 shows that the detection of relativistic ions up to $Z = 6$ is feasible with 4-gap MtRPCs operated at typical fields ($E = 100$ kV/cm), with a resolution $\sigma_r \simeq 80$ ps, and $\varepsilon \simeq 100\%$. A more detailed differential study as a function of the energy loss is presented in the next section.

4. Dependence with particle type

4.1 Introduction

At fixed momentum per nucleon ($\gamma\beta$ constant), heavy charged particles lose energy due to electromagnetic interactions in square proportion to its electric charge according to the Bethe-Bloch formula:

$$\frac{dE}{dx} = K \left(\frac{Z_m}{A_m} \right) Z^2 \frac{1}{\beta^2} \left[\frac{1}{2} \ln \frac{2m_e c^2 \beta^2 \gamma^2 T_{max}}{I^2} - \beta^2 \right] \quad (4.1)$$

where Z_m, A_m are the atomic and mass number of the medium, m_e is the electron mass, I the mean excitation energy, and $K = 0.307075$ MeVg⁻¹cm². A prescription for calculating Z_m/A_m and I in mixtures according to [38, 39] will be used in the following.

Using fully stripped ions of charge Z is a practical alternative to study the energy loss dependence of a counter over a very broad dynamic range. Moreover, as long as measurements are performed in the forward beam direction any low- Z fragment is likely to proceed from spallation reactions, roughly keeping its energy per nucleon (E_K/A) and so β . Therefore in the present experimental situation, having a primary C¹² beam with $Z = 6$, it is reasonable to assume that ions with $Z=1-6$ will have a primary ionization in a relative proportion close to 1, 4, 9, 16, 25, 36. Additionally, for the energies $E_K/A = 1.8$ GeV used here, even in the very unlikely case that a secondary proton (for instance) would travel forward with a kinetic energy as low as $E_{K,p} = 1/4(E_K/A)$, it would release only 20% more energy than mips according to eq. 4.1. The above considerations are true only for electromagnetic interactions with hadronic interactions expected to happen only residually. In our setup we have no way to separate contributions from hadronic interactions but with another reference detector placed RPC downstream, one could separate those by vetoing on it. We will disregard the effect of hadronic interactions for the latter discussion and so, being $\gamma\beta \simeq 2.7$ it will be useful to re-express the Z -dependence as $\Delta E/\Delta E_{mips} = Z^2$.

4.2 Charge distribution

To the authors knowledge, there is only one published work on the energy loss dependence of MtRPCs [24], whose conclusions yet remain disputed, specially regarding the very high shifts observed for the average time of flight \bar{t} as compared with the expected one [25]. We revisited the situation starting from the dependence of the average prompt charge \bar{q}_p with the energy loss. For that we took the average charge for protons as a function of the momentum p from Fig. 8 in ref. [24] and pad-ring 3 that corresponds to perpendicular incidence, according to the authors. The Bethe-Bloch formula for the HARP gas mixture was evaluated from eq. 4.1 and used for recalculating $\Delta E/\Delta x$, re-normalizing its value to the value for mips. Since the average prompt charge is referred in arbitrary units in [24] we arbitrarily re-scaled it to provide the best agreement with our data. Note that the geometry of the HARP cells is very close to the HADES one, having also 4

gaps and a very similar gap spacing ($g = 0.3\text{mm}$ and $g = 0.28\text{mm}$, respectively). Values for HARP are shown in Fig. 14-left (squares).

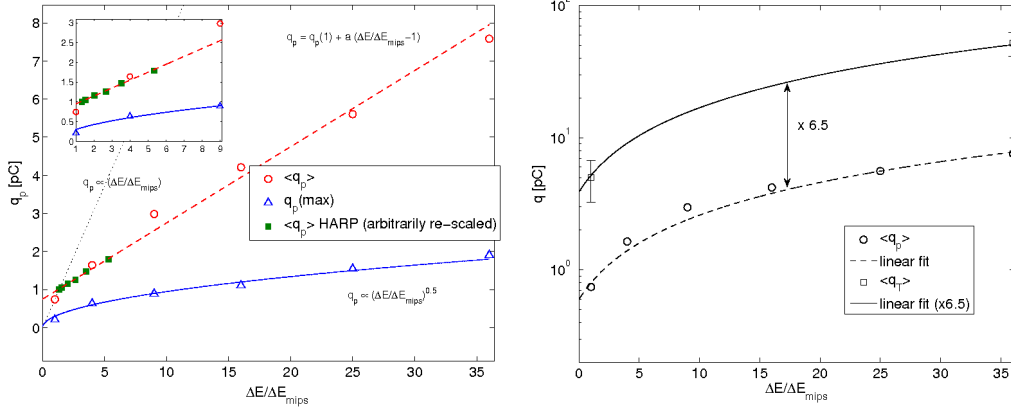


Figure 14. Left: average prompt charge \bar{q}_p (circles) and charge at maximum $q_p(\text{max})$ (triangles) from the RPC as a function of the energy loss expressed in mips units. Data from HARP is shown for comparison. Different trend curves are indicated. Right: average prompt \bar{q}_p and total \bar{q}_T charge (circles, squares) as a function of the energy loss expressed in mip units. A linear fit is shown (dashed line) together with the same curve re-scaled by a factor 6.5 to meet the \bar{q}_T data.

When increasing the energy loss the probability of streamers also increases [23]. The above fact makes the interpretation of the charge spectra difficult since a theoretical description of streamers in RPCs is not yet available. In order to simplify this task we used the fits to Landau-like functions of Fig. 11 to extract the charge at maximum $q_p(\text{max})$ whose energy loss dependence is expectedly dominated by the avalanche dynamics and little dependent on the streamer mechanism. The values for $q_p(\text{max})$ together with the direct charge average \bar{q}_p are shown in Fig. 14-left. The trends of $q_p(\text{max})$ and \bar{q}_p are indeed similar up to $\Delta E/\Delta E_{mips} = 4$ but diverge afterwards, pointing to the influence of streamers for $\Delta E/\Delta E_{mips} > 4$. Note the reasonable good agreement in the trend of \bar{q}_p when comparing with the HARP data. The following phenomenological curves could be found:

$$q_p(\text{max}) \propto \sqrt{\frac{\Delta E}{\Delta E_{mips}}} \quad (4.2)$$

$$\bar{q}_p = \bar{q}_p(1) + 0.2 \left(\frac{\Delta E}{\Delta E_{mips}} \right) \quad (4.3)$$

As a result of Space-Charge, neither $q_p(\text{max})$ nor \bar{q}_p show a proportional behavior with the primary ionization.

Since the total current and particle rates were continuously monitored (Fig. 5) the total average charge \bar{q}_T could be determined to be $\bar{q}_T = 5 \pm 1$ pC under proton irradiation and $\bar{q}_T = 53 \pm 10$ pC for C^{12} under C^{12} irradiation. The latter calculation requires to re-estimate the proportion of C^{12} ions in the measured rate, and is done from Fig. 6, yielding 3/5 of the total. The contribution of He and proton ions to the measured current is neglected. Note that if we assume the same scaling with the energy loss for \bar{q}_T than for \bar{q}_p the He and p rates (2/3 of the total) contribute to the measured

current in less than 10%. From run to run variations we estimated in 20% the error in \bar{q}_T for protons and the same uncertainty was taken for the C^{12} value. Data for \bar{q}_p and \bar{q}_T is shown as a function of $\Delta E/\Delta E_{mips}$ in Fig. 14-right together with a linear fit to the \bar{q}_p data. The same function can describe the trend of the \bar{q}_T points after multiplying by a factor $\times 6.5$. If a model of the kind of [15] would be used for describing avalanche multiplication under strong Space-Charge, the ratio \bar{q}_T/\bar{q}_p is indeed expected to depend on the initial energy loss, because the higher the initial charge the earlier the avalanche enters in the Space-Charge regime and the more the released electrons drift before arriving to the anode, resulting in a higher electron-induced charge for the same avalanche charge. Because of that, and because of the different behavior of \bar{q}_p and $q_p(\max)$ with $\Delta E/\Delta E_{mips}$, we believe that the scaling observed in Fig. 14-right is strongly affected by the presence of the streamers.

4.3 Time distribution

A striking observation in [1] was the existence of very strong drifts of the average time-of-flight as a function of the energy loss. The much larger range of ionizations present here allows us to discuss this point in high detail. First, in Fig. 15-left the time resolution after slewing correction is shown for the different species at $V = 5.6$ kV. The analytical scaling from eq. 1.2 is illustrated by fixing $\sigma_T(1)$ to be 80 ps. Unfortunately, the scaling of σ_T is not visible in data, pointing to the fact that a limitation to the resolution different from avalanche dynamics is present in the measurements. In connection with this observation it must be recalled that despite the solid derivation of eq. 1.2 there is no systematic experimental study so far on the behavior of σ_T with the energy loss. Proving (or disproving) the scaling of eq. 1.2 by systematic measurements would be extremely important in order to better understand the practical limitations of these counters for timing. An experimental confirmation of this scaling would allow to understand why, in practice, the difference between 1-gap counters and multi-gap can be as little as $\sigma_T = 55$ ps (1 gap, [43]) and $\sigma_T = 40$ ps (10 gaps, [2]), when operated in very similar conditions of gas mixture and field. No data from the HARP collaboration is available on this important aspect. Since our system is limited to a resolution of $\sigma_T = 40$ ps for the mean-time (Fig. 8) a much more accurate FEE+TDC chain would be needed, nevertheless, in order to evaluate the theoretical prediction for C^{12} ions.

Fig. 15-right shows the average behavior of $\langle \Delta t_{RPC-S_o} \rangle$ (eq. 3.3) before corrections and referred to the case of mips (circles), together with the analytical scalings from eq. 1.1 assuming $t_{rise} = 300$ ps (dashed line). Despite the reasonable value obtained for t_{rise} this is indeed the minimum value consistent with the observations: if a sizeable drift is present in the reference scintillators part of the drift originated in the RPC would be effectively shadowed after taking the difference. In the absence of constant fraction discriminators the best practical approach to estimate this effect in the scintillators is by looking at the $\Delta t_{S_o-S_1}$ distributions when the particle releases charges corresponding to $Z=1-6$ in S_o and keeping a narrow cut around $Z=1$ in S_1 . The above value can be used to correct $\langle \Delta t_{RPC-S_o} \rangle$ from the scintillator drifts and provide an estimate of the time drift caused by the RPC alone (triangles). The latest HARP data from [25] are also overlaid (squares) after an arbitrary shift. According to the authors the values have been obtained after a re-analysis based on a direct determination of the momentum p by physical constraints (elastic scattering) and are expected to be free from artificial drifts that previously arose from an incorrect momentum reconstruction. In order to compare with present data the energy loss was

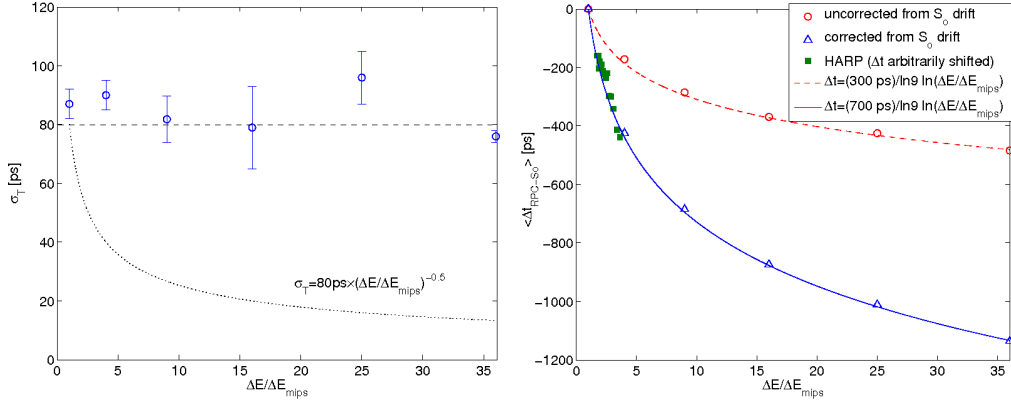


Figure 15. Left: Time resolution σ_t as a function of the energy loss expressed in mips units together with the approximate $1/\sqrt{\Delta E}$ scaling. Right: average time of flight between RPC and scintillator S_o as a function of the energy loss expressed in mips units together with the approximate $\ln(1/\Delta E)$ scaling before (circles) and after (triangles) correcting for the scintillator drift. HARP data is shown as full squares. Two theoretical curves are fitted in each case with a single parameter $t_{rise} = 300$ ps (dashed line) and $t_{rise} = 700$ ps (continuous line).

re-calculated from eq. 4.1, as in previous sub-section. Several things can be noted: i) despite the different FEE band-widths the corrected values for Δt_{RPC-S_o} agree with latest HARP data and can be described with a logarithmic dependence if $t_{rise} = 700$ ps; ii) surprisingly, the authors in [25] implicitly assumed a value for $t_{rise} = 100$ ps for the discussion in the paper, presumably inspired by theoretical values for $(\alpha - \eta)v_e$, despite this seems to be largely inconsistent with their own measurements; iii) the previously reported ‘500 ps’ effect from [24] can also not be confirmed by the present measurements; iv) a lower limit for $t_{rise} > 300$ ps readily arises from the present data.

For the sake of completeness, fig. 16-right shows the detector efficiency as a function of the energy loss. The fact that for $Z > 1$ the efficiency is almost 100% indicates that the trigger geometry is reasonable, being the lower values for $Z = 1$ partly attributable to the slightly low operating voltage (Fig. 12). Fig. 16-left presents the specie population after cuts.

5. Discussion

5.1 Element identification

When aiming at ion identification a time of flight measurement provides the ratio $\gamma\beta = p/A$ while momentum (p) and element (Z) identification must be done by independent means [14]. So it is interesting to see at which extent a MtRPC has resolving power in Z by using the q_p information. In order to evaluate this we define the purity P against ion Z_2 for a 90% identification efficiency of ion Z_1 by:

$$P_{90} = \left(\frac{N_{Z_1} - N_{Z_2}}{N_{Z_1}} \right)_{\varepsilon_{Z_1}=90\%} \quad (5.1)$$

where the condition $\varepsilon_{Z_1} = 90\%$ imposes a fixed cut in the prompt charge. Taking all the populations from the normalized distributions of Fig. 11 the suppression factor Π_{90} for specie Z_2 when aiming

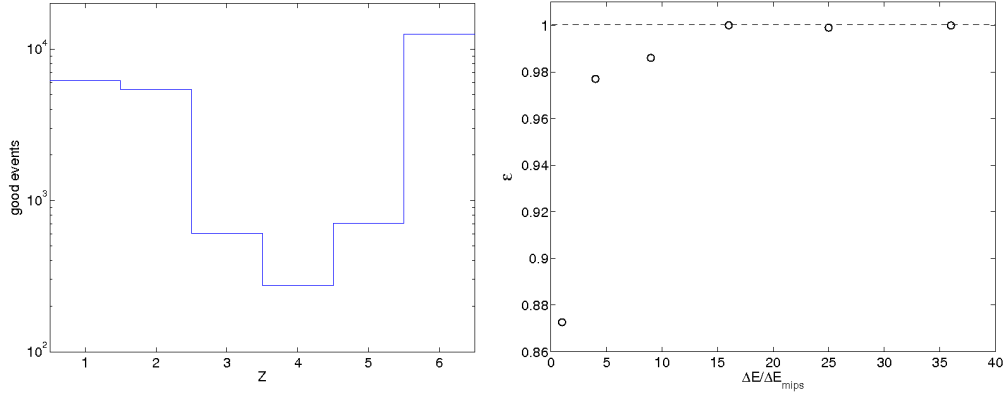


Figure 16. Left: population of ions with charge states 1 – 6 after cuts ('good events'). Right: detection efficiency as a function of the energy loss expressed in mips units. The points have being obtained for $V = 5.6$ kV at low particle rates ($\phi < 10$ Hz/cm²).

at detecting Z_1 with 90% efficiency can be defined as:

$$\Pi_{90} = \left(\frac{N_{Z_1}}{N_{Z_2}} \right)_{\epsilon_{Z_1}=90\%} = \frac{1}{1 - P_{90}} \quad (5.2)$$

Π_{90} is shown in Fig. 17 for the different ions.

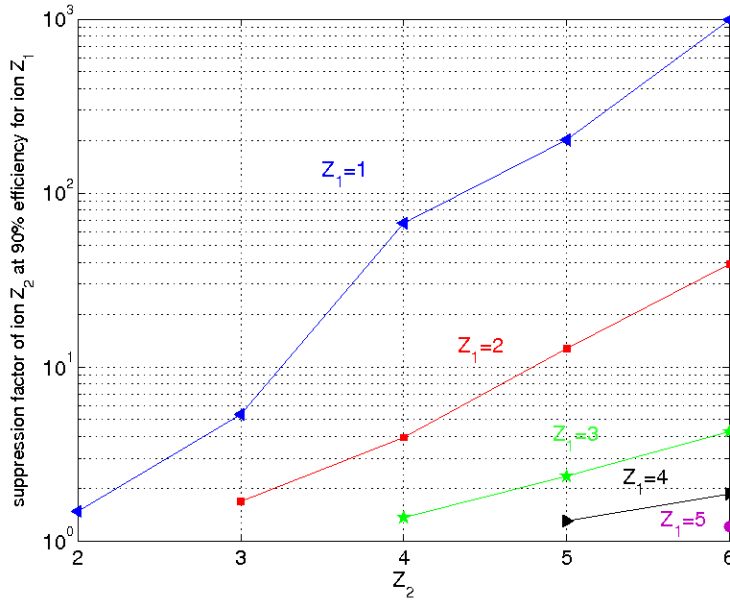


Figure 17. Suppression factor of element in charge state Z_2 when imposing a cut in the RPC charge for a 90% identification efficiency of element in charge state Z_1 . The suppression factor has been obtained after fitting the charge distributions to Landau-like functions.

The overall suppression is modest, but a strong suppression already exists for $Z = 4$ ions when aiming at proton detection ($\sim \times 65$). Contrary, the suppression of alpha particles for proton

detection as well as that of $Z = 6$ ions for $Z = 4$ ion detection is only slightly higher than 1.

5.2 Time-Charge correlation

Slewing correction is the procedure after which the time of flight walk as a function of the signal amplitude is corrected for. The nature of this correlation is not yet clear, but it seems to be dominated by the electronic response at low charges [16]. Indeed very little correlation, if any, remains in the present case for $Z = 6$, where the signals are largely above threshold (Fig. 18-up), unlike protons. Moreover, the measured time for high charges is systematically shifted by roughly 400 ps when comparing protons and Carbon, as already discussed in connection with Fig. 15. In this particular case the external detectors provide a clean separation in Z so that the time distributions corresponding to the different ions can be identified and the drift of the average time becomes a trivial systematic effect. Now, if Z is not known (or, generally, if $\Delta E/\Delta E_{mips}$ is not known), this systematic dependence of the average time can not be fully corrected for and these variations enter effectively in the measured response function.

The worsening of the time resolution due to variations in the average time due to different primary ionizations is known since time [19] but has only been applied to account for the Poisson fluctuations in the initial number of clusters. Following the spirit of this work, a simple although more experimentally-driven approach is devised here to estimate this effect in practice. Let's assume first that the time resolution does not depend or depends little on the average ionization. This assumption is not supported by avalanche models, but would be the case if the measured resolution is not dominated by the detector response function but by an external source (FEE jitter, noise and/or TDC resolution). We think that this case is practically relevant. Further, we assume a flat distribution of possible energy losses over a range $\Delta E_{max} - \Delta E_{mips}$. The rms of the resulting distribution can be estimated from the relations:

$$\bar{t}_{\Delta E} = \frac{1}{\Delta E_{max} - \Delta E_{mips}} \int_{\Delta E_{mips}}^{\Delta E_{max}} \frac{t_{rise}}{\ln 9} \frac{\Delta E_{mips}}{\Delta E} d\Delta E \quad (5.3)$$

$$\sigma_T^2 = \frac{1}{\Delta E_{max} - \Delta E_{mips}} \int_{\Delta E_{mips}}^{\Delta E_{max}} \left[\left(\frac{t_{rise}}{\ln 9} \frac{\Delta E_{mips}}{\Delta E} \right)^2 - \bar{t}_{\Delta E}^2 \right] d\Delta E \quad (5.4)$$

$$(5.5)$$

that yield:

$$\sigma_T(\Delta E_{max}) = \frac{t_{rise}}{\ln 9} \sqrt{1 - \frac{1}{\left(\frac{\Delta E_{max}}{\Delta E_{mips}} - 1\right)^2} \frac{\Delta E_{max}}{\Delta E_{mips}} \ln^2 \frac{\Delta E_{max}}{\Delta E_{mips}}} \quad (5.6)$$

Eq. 5.6 has the curious property of tending asymptotically to $t_{rise}/\ln 9$ for high energy deposition. Since the intrinsic detector resolution is expected to be of this order (eq. 1.2) in the limit of low ionization, one may conclude that energy spread cannot modify the detector resolution by a large factor. In reality two things can happen: i) that the intrinsic detector resolution from eq. 1.2 is reached, and then from eq. 5.6 the worsening due to the energy loss will be of the same order than the resolution itself, being the latter partially compensated by the improvement in the intrinsic resolution for every value of ΔE (eq. 1.2) or ii) that it is not reached, and then the deterioration from eq. 5.6 will be smaller than the resolution itself, anyway. So it seems that the variations on the initial ionization are called to be 'second order' for the counter resolution. The above considerations

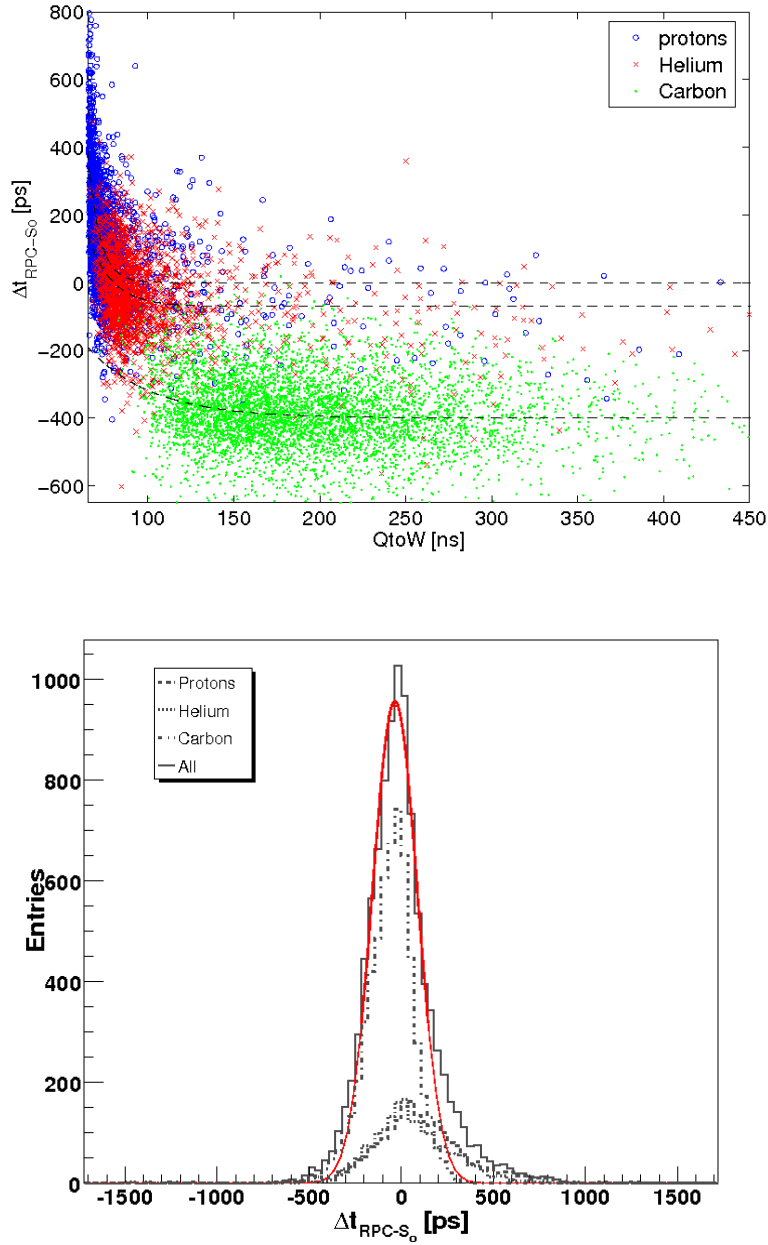


Figure 18. Up: Scatter plot (color on-line) showing the walk of the time-of-flight between RPC and scintillator S_0 as a function of the signal width ($QtoW$) for protons (\circ), Helium (\times) and Carbon (\cdot). Tendency curves are shown in each case. Down: time-of-flight distribution after applying a unique slewing correction for all species (ignoring external identification in Z). Identification is applied at the end of the procedure to evaluate the result in such conditions. A resolution $\sigma_\tau = 115$ ps is obtained for the combined fit, with increased tails towards delayed times as compared with the case where identification in Z is provided.

cannot account for all the possible ΔE distributions and must be taken with care when a highly Gaussian response is needed. Relevant cases where this effect should be taken into account are neutron or γ detection due to interaction in the electrodes, where a secondary particle with its

corresponding energy distribution is released, and also ion detection. So, the usual assumption that a higher ionization renders a better time resolution can not be considered universally true for this kind of detectors, on the basis of the existing knowledge. A detailed discussion on this effect can be found in [44].

Another relevant situation would be the dependence of the average ionization with Z , assuming the energy per nucleon to be the same for all the particle species. Let's further assume that $2N + 1$ species are present in the same amount, centered around specie \bar{Z} . If a detector providing identification in Z would not exist an extra jitter will appear in the form:

$$\bar{t}_{\bar{Z}} = -\frac{t_{rise}}{\ln 9} \left(\sum_{i=1}^N \frac{\ln(\bar{Z} + i)^2 + \ln(\bar{Z} - i)^2}{2N + 1} + \frac{\ln \bar{Z}^2}{2N + 1} \right) \quad (5.7)$$

$$\sigma_t^2 = \left(\frac{t_{rise}}{\ln 9} \right)^2 \sum_{i=1}^N \frac{\left(\ln(\bar{Z} + i)^2 - \frac{\ln 9}{t_{rise}} \bar{t}_{\bar{Z}} \right)^2 + \left(\ln(\bar{Z} - i)^2 - \frac{\ln 9}{t_{rise}} \bar{t}_{\bar{Z}} \right)^2}{2N} \quad (5.8)$$

in the limit where \bar{Z} and N are big, but still $\bar{Z} \gg N$, eq. 5.8 yields:

$$\sigma_t(N, \bar{Z}) = \sqrt{\frac{8}{6} \frac{t_{rise}}{\ln 9} \frac{N}{\bar{Z}}} \quad (5.9)$$

so the practical influence of the uncertainty in Z in the measured resolution is also little for high \bar{Z} values. However, for cases where $\bar{Z} \simeq N \simeq 1$ (the present case) the jitter arising from a bad identification in Z will be as high as 500 ps, as illustrated in Fig. 18. As a benefit, the Z -resolving power of the RPC itself will be also much higher, resulting in a time-charge correlation curve different from the usual one for mips (compare circles in Fig. 18 with all the three species together). In particular, if only Carbon and protons would be present in our sample they can very easily identified and corrected for, and only few events (Carbon with $QtoW < 100$ ns and protons with $QtoW > 100$ ns) would be wrongly identified. If we would have ignored for a while, in this particular experimental conditions, the existence of secondary particles arising from the primary C beam, and would have used a single correlation curve the net result would have been a deterioration of the estimated time resolution for C ions from $\sigma_t = 73$ ps to $\sigma_t = 115$ ps, with large tails towards delayed times.

5.3 Space-Charge

There is a simple analytical model that accounts for Space-Charge effects, and that is based on the avalanche equations in the presence of a charge-dependent Townsend coefficient [15]. This model is analytical for each avalanche and depends on its position and initial ionization, but the solution to the general problem can only be treated numerically. It is not the purpose of the present work to quantitatively describe Space-Charge, but we did some clarifying attempt by evaluating formulas in [15] for three typical avalanche positions in the gap. Further, the simplifying assumption that all the charge is released at the position of the avalanche is done. We took values $\alpha^* = 73 \text{ mm}^{-1}$, $n_o/\text{gap} = 3\Delta E/\Delta E_{mips}$, $q_{sat} = 10^5$ (number of electrons for a 50% drop of α^*) and leave the overall normalization as a free parameter to match the data. Finally, we looked at three situations (Fig. 19): i) the avalanche is produced in the cathode ($x_o = 0$, dotted line), ii) in the center of the gap ($x_o = g/2$, dashed) and iii) $20\mu\text{m}$ separated from the anode (dot-dashed).

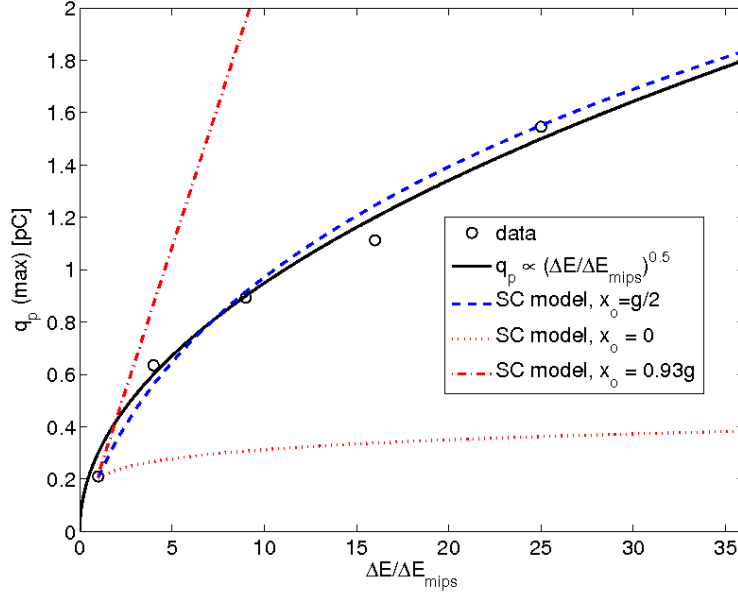


Figure 19. Measured charge at maximum $q_p(\max)$ as a function of the energy lost in mips units (circles). The $\sqrt{\Delta E}$ experimental scaling is shown together with the evaluation of the model of Fonte [15] under the assumptions of the text, for three different positions x_o of the avalanche inside the gap (center, close to the cathode and close to the anode).

Clearly, we cannot conclude from the comparison shown in Fig. 19 by such a simplified model, but we can illustrate how Space-Charge works. For avalanches produced close to the cathode there is almost no sensitivity to the initial ionization, since its evolution is anyway doomed to a similar end once the critical value of q_{sat} is reached. For avalanches produced close to the anode, the resulting charge will be obviously rather small (an effect absorbed here in the overall normalization) but essentially proportional to the initial one, since the avalanche charge is then much smaller than q_{sat} and Space-Charge plays no role. For the center of the gap, an intermediate situation is reached, where the avalanche growth is modified but some sizeable correlation with the initial charge is still present. Remarkably, this latter situation matches well the trend of the experimental points.

5.4 Streamers

From the experimental point of view when aiming at ion detection it would be probably convenient to operate the detector in absence of streamers. It is possible to perform a semi-quantitative evaluation of what is the practical implication of this fact by using some classical arguments: if we denote by α_c^* the effective gain threshold at which streamers would arise, then following the approximate derivation of [45] it can be seen that this value will depend on the initial ionization as:

$$\alpha_c^*|_Z = \alpha_c^*|_{mips} - \frac{\ln Z^2}{g} \quad (5.10)$$

so, the critical value of the Townsend coefficient for an ion with charge Z is naturally lower than that of mips, and the same will happen for the field at which streamers will appear in one case and the other. Now we can further assume a dependence of $\alpha^*(E) \simeq \frac{d\alpha}{dE}E - b$ (inspired by transport

codes [16]) and obtain the necessary decrease in the field to operate the chamber in the absence of streamers that would simply be, for a given ion Z :

$$E[\text{kV/cm}] = \frac{dE}{d\alpha} [\alpha_c^*|_{mips} - 1/g \ln Z^2 + b] \quad (5.11)$$

if we make the natural assumption $\alpha_c^*|_{mips} \simeq \alpha^*(E_o = 100 \text{ kV/cm})$ then:

$$E_z[\text{kV/cm}] = E_o[\text{kV/cm}] - \frac{dE}{d\alpha} \left[\frac{\ln Z^2}{g} \right] \quad (5.12)$$

as a function of Z . By directly substituting the simulated value for $\frac{dE}{d\alpha}$ [16] it can be expected that even for the most extreme case of Au detection ($Z = 79$) a mere decrease of a 10% in the field would be sufficient to operate the chamber in pure avalanche mode, and the anticipated decrease of performances resulting from the lower field would be over-compensated if the scalings with Z illustrated through eqs. 1.2 and 1.3 hold:

$$\sigma_r(Z) \simeq \frac{K_1 t_{rise}}{Z \ln 9} \quad (5.13)$$

$$\varepsilon(Z) > 1 - \exp \left[-n_o \left(1 - \frac{\eta}{\alpha} - \frac{\ln(1 + \frac{(\alpha-\eta)n_{th}}{E_w})}{\alpha g} \right) Z^2 \right] \quad (5.14)$$

since t_{rise} and α have approximate linear dependences with the field E .

6. Conclusions

A time resolution $\sigma_r \simeq 80 \text{ ps}$ at $\varepsilon \simeq 100\%$ has been consistently measured for relativistic ions with charge states $Z=2-6$ for the first time by just using standard ‘off the shell’ Multigap timing RPCs from the HADES wall.

The energy loss dependence of the avalanche charge and detector-related time-of-flight systematic shifts have been compared with previous data and extended over a much larger range of primary ionizations, showing a reasonable agreement. The measured time drifts cannot be accommodated in the existing theoretical framework unless a value for the signal rise-time 2.5 times bigger than current experimental estimates is assumed. The observed behavior of the prompt charge with the initial ionization seems to provide a stringent benchmark for the parameters of Space-Charge models and a simple comparison was attempted, showing a reasonable agreement.

Operation up to Carbon fluxes of 100 Hz/cm^2 was demonstrated with $\sigma_r < 100 \text{ ps}$ and $\varepsilon \simeq 100\%$ under an 8-second spill (50% duty cycle) and $\simeq 2 \times 2 \text{ cm}^2$ irradiated area. Above 100 Hz/cm^2 the time resolution deteriorates rapidly but the efficiency was kept up to 600 Hz/cm^2 (at least) due to the much higher initial ionization as compared with mips. The behavior of the resolution as a function of the flux is similar to that of mips, when re-scaling the rate by a factor $\times 5$. This value is very similar to the measured ratio of the total charges $\bar{q}_{T,C12}/\bar{q}_{T,p} = 6.5$, as expected from a simple DC modelling of the detector. Based on this observation, the measured trend of $\bar{q}_r(Z)$ can be extrapolated to high Z , yielding an approximate dependence for the rate capability as $\Phi_{max}(Z) = \frac{1 \text{ kHz}}{0.2Z^2}$, that would severely limit the operating rate to barely 1 Hz/cm^2 for Au ions. Based on the present measurements, it is likely that the very high initial charge will not affect the chamber stability in

such situation but it will largely reduce its rate capability. In a realistic application, the working voltage should be chosen taking this fact into account.

The nature of the time-charge correlation and the practical timing limitations when the energy loss of the ionizing particle can not be addressed by external means have been discussed. It has been shown that under reasonable assumptions the detection of particles through secondary processes (in case of neutron or γ -photons, for instance) would yield an extra time jitter of the order of the detector intrinsic resolution for mips, therefore the good timing characteristics of these devices will be preserved even in such a situation. A practical example has being given based on the present data. Nevertheless, the intuition that higher ionization yields better results does not seem to be a trivial statement for these counters and every physical case should be probably addressed experimentally.

Despite the large dynamic range explored here the chamber+electronics performed stably during the whole experiment, underlining the superior performance of float glass Multi-gap timing RPCs in highly ionizing environments when high rates are not required. Always depending on the Z of the species of interest, a Multi-gap configuration does not seem to be mandatory for ion detection. A more practical RPC design could be probably based on 1-gap RPCs (single or mirrored [46]).

Acknowledgments

This work is supported by EU/FP6 contract 515876 and Xunta project PGIDT06 PXIC 296091PM (Galicia-Spain). The authors would like to acknowledge the professional help of E. Schwab and T. Heinz.

References

- [1] V. Ammosov et al., Nucl. Instr. and Meth. A 578(2007)119.
- [2] A. N. Akindinov et al., Nucl. Instr. and Meth. A 533(2004)93.
- [3] W. Yi et al., Nucl. Instr. and Meth. A 538(2005)425.
- [4] A. Shuetttauf, Nucl. Phys. B (Proc. Suppl.) 158(2006)47.
- [5] D. Belver et al., Nucl. Instr. and Meth. A 602(2009)687.
- [6] P. Senger, Phys. Part. Nucl. 39(2008)1055.
- [7] V. V. Parkhomchuck, Yu. N. Pestov, N. V. Petrovykh, Nucl. Instr. and Meth. A 93(1971)269.
- [8] R. Santonico and R. Cardarelli, Nucl. Instr. and Meth. A 187(1981)377.
- [9] E. Cerron Zeballos et al., Nucl. Instr. and Meth. A 374(1996)132.
- [10] P. Fonte, A. Smirnitski, M. C. S. Williams, Nucl. Instr. and Meth. A 443(2000)201.
- [11] A. Blanco et al., Nucl. Instr. and Meth. A 485(2002)328.
- [12] A. Blanco et al., IEEE Trans. Nucl. Sci. 53(2006)2489.
- [13] R³B, Technical Proposal, GSI, Dec. 2005.

http://www.gsi.de/forschung/kp/kr/R3B/Technical_Proposal.pdf.

- [14] H. Alvarez-Pol et al., Nucl. Phys. B (Proc. Suppl.) 158(2006)186.
- [15] P. Fonte, Nucl. Instr. and Meth. A 456(2000)6.
- [16] C. Lippmann, W. Riegler, Nucl. Instr. and Meth. A 517(2004)54.
- [17] M. Abbrescia, Nucl. Instr. and Meth. A 431(1999)413.
- [18] A. Gobbi, A. Mangiarotti, Nucl. Instr. and Meth. A 508(2003)23.
- [19] A. Mangiarotti, P. Fonte, A. Gobbi, Nucl. Instr. and Meth. A 533(2004)16.
- [20] A. Mangiarotti et al., Nucl. Phys. B (Proc. Suppl.) 158(2006)118-122.
- [21] W Riegler, C. Lippmann, Nucl. Instr. Meth. A 518(2004)86.
- [22] P. Fonte et al., IEEE Trans. Nucl. Sci. 49(2002)881.
- [23] D.Gonzalez-Diaz, PhD Thesis(chapter VII), Santiago de Compostela 2006,
http://jinst.sissa.it/jinst/theses/2006_JINST_TH_003.jsp.
- [24] M. Bogomilov et al., IEEE Trans. Nucl. Sci. 54(2007)2.
- [25] V. Ammosov et al., Nucl. Instr. Meth. A 602(2009)639.
- [26] A. Blanco, P. Cabanelas et al., Nucl. Instr. and Meth. A 602(2009)691.
- [27] H. Stelzer, Nucl. Instr. and Meth. 133(1976)409.
- [28] A. Breskin, N. Zwing, Nucl. Instr. and Meth. 144(1977)609
- [29] R. Ganz et al., Nucl. Instr. and Meth. A 432(1999)379.
- [30] D. Belver et al., Nucl. Instr. Meth. A 602(2009)713.
- [31] A. Gil et al., T11001 JINST 2(2007).
- [32] A. Gil et al., ‘Distributed Low Voltage System for the Front-End of the HADES timing RPC wall’,
accepted in IEEE Trans. Nucl. Sci.
- [33] I. Frohlich et al., IEEE Trans. Nucl. Sci. 55(2008)59.
- [34] W. Koenig, J. Pietraszko, ‘Diamonds as fast timing detectors for MIPS: The HADES proton-beam
monitor/start detector’, communication at DPG spring meeting, Bochum, 2009.
- [35] G. Aielli et al., Nucl. Instr. and Meth. A 456(2000)82.
- [36] D. Gonzalez-Diaz, P. Fonte, J. A. Garzon, A. Mangiarotti, Nucl. Phys. B (Proc. Suppl.) 158(2006)111.
- [37] D.Gonzalez-Diaz, M. Morales et al., Nucl. Instr. and Meth. A 602(2009)713.
- [38] C. Amsler et al., Phys. Let. B667, 1(2008).
- [39] Sternheimer et al., Atomic and nuclear data tables, 30(1984)261.
- [40] H. Alvarez-Pol et al., Nucl. Instr. and Meth. A 535(2004)277.
- [41] P. Fonte et al., PoS, HEP2005(2005)376.
- [42] D. Gonzalez-Diaz et al., Nucl. Instr. and Meth. A 555(2005)72.
- [43] A. Blanco et al., Nucl. Instr. and Meth. A 478(2002)170.
- [44] C. Lippmann, H. Vincke, W. Riegler, Nucl. Instr. and Meth. A 602(2009)735.
- [45] H. Raether, “Electron avalanches and breakdown in gases”, Butterworths, London, 1964.
- [46] E. Casarejos, talk at R3B collaboration meeting, October 2008, GSI.